Real-time Multi-length Scale Chemical Tomography of Fixed Bed Reactors during the Oxidative Coupling of Methane

Antonis Vamvakeros[1,2,3*], Dorota Matras[2,4], Simon D. M. Jacques[3*], Marco di Michiel[5], Stephen W. T. Price[3,6], Pierre Senecal[1,2], Miren Agote Aran[1,2], Vesna Middelkoop[7], Gavin B. G. Stenning[8], J. Frederick W. Mosselmans[6], Ilyas Z. Ismagilov[9], Andrew M. Beale[1,2,3*]

[1] Department of Chemistry, University College London, 20 Gordon Street, London, WC1H 0AJ, UK.

[2] Research Complex at Harwell, Harwell Science and Innovation Campus, Rutherford Appleton Laboratory, Didcot, Oxon, OX11 0FA, UK.

[3] Finden Limited, Merchant House, 5 East St Helen Street, Abingdon, OX14 5EG, UK.

[4] School of Materials, University of Manchester, Manchester, Lancashire M13 9PL, UK.

[5] ESRF- The European Synchrotron, Grenoble, 38000 France.

[6] Diamond Light Source, Harwell Science and Innovation Campus, Didcot, Oxon, OX11 0DE, UK

[7] Flemish Institute for Technological Research, VITO NV, Boeretang 200, 2400 Mol, Belgium

[8] ISIS Neutron and Muon Source, Rutherford Appleton Laboratory, Didcot, OX11 0QX, UK.

[9] Boreskov Institute of Catalysis SB RAS, Pr. Akademika Lavrentieva 5, 630090 Novosibirsk, Russia.

Correspondance email: antony@finden.ac.uk, simon@finden.ac.uk, andrew.beale@ucl.ac.uk

Abstract

In this work, we present the results from multi-length-scale studies of a Mn-Na-W/SiO_2 and a La-promoted Mn-Na-W/SiO_2 catalyst during the oxidative coupling of methane reaction. The catalysts were investigated from the reactor level (mm scale) down to the single catalyst particle level (μm scale) with different synchrotron X-ray chemical computed tomography techniques (multi-modal chemical CT experiments). These *operando* spatially-resolved studies performed with XRD-CT (catalytic reactor) and multi-modal µ-XRF/XRD/absorption CT (single catalyst particle) revealed the multiple roles of the La promoter and how it provides the enhancement in catalyst performance. It is also shown that non-crystalline Mn species are part of the active catalyst component rather than crystalline Mn_2O_3 / Mn_7SiO_{12} or $MnWO_4$.

Keywords: imaging; xrd; operando; catalyst; xrf; micro; in situ;

Introduction

Numerous technological advances achieved over the past decade have made the extraction of natural gas from unconventional deposits possible; this achievement is expected to have a direct impact on the chemical industry in the not-so-distant future [1,2]. Methane, which is the main component of natural gas, shale gas and renewable biogas, is considered to be an abundant hydrocarbon, yet underused, resource when compared to crude oil [3]. As such, there is a strong economic imperative to develop industrially relevant technologies for environmentally-friendly and cost-effective direct conversion of methane to higher value bulk chemicals [4–6]. A possible route to achieve this goal is through the oxidative coupling of methane (OCM) reaction which leads to the formation of ethylene, one of the building blocks of the chemical industry [7–9]:

$$2CH_4 + O_2 \rightarrow C_2H_4 + 2H_2O \qquad \Delta H^\circ_{298K} = -282 \text{ kJ mol}^{-1}$$

In general, high temperatures (i.e. typically above 750 °C) are required for the OCM reaction due to the chemical stability of the methane molecule (energy of ca. 438 KJ mol^{-1} is required to break the C-H bond)[10]. In order for the OCM reaction to be an economically viable technology for industrial applications, the solid catalyst must exhibit both high methane activity and selectivity to C_2 molecules and also long-term chemical stability under the required high temperatures. It is generally accepted that the most promising OCM catalysts are the Mn-Na-W/SiO_2 based materials as such catalysts exhibit high performance under OCM reaction conditions (>20 % yield for C_2 molecules at 800 °C) [10,11]. Although this family of catalysts has been extensively investigated over the past 25 years, there is still much debate regarding the nature of the active phases/species, chemical stability, role of promoters, preferred method of preparation, optimal weight loading of the different elements and even the reasons behind the deactivation of these catalysts[12–14]. In a review paper by Arndt *et al.*[13]

it was suggested that a synergistic effect between Mn, Na and W must be responsible for the catalyst activity, however lack of *in situ* or *operando* studies regarding these complex multi-component catalysts allows only for the speculations on the nature of active sites [14].

Fang *et al.* were the first to develop the $Mn-Na_2WO_4/SiO_2$ as a catalyst for the OCM reaction [15,16]. The nature of the active sites in this complex multi-component catalyst was mainly investigated during the 90s. In the study of Sofranko *et al.* the performance of various transition metal oxides (i.e. 5 wt. % metal loadings) was examined in a cyclic redox mode [17]. Mn_2O_3/SiO_2 was found to be the best catalyst in terms of stability and productivity; the species responsible for the high selectivity to C_2 were considered to be Mn_2O_3 or Mn-O-Si species. Ji *et al*. showed that the best performance, regarding the methane conversion and C_2 selectivity was achieved in the trimetallic $Mn-W/SiO_2$ catalyst promoted with alkali metals ions (Na and K) [18]. More importantly, the presence of Na and K resulted in the enrichment of catalyst surface with tetrahedral WO_4 species, responsible for methane activation. In literature, two distinct theories regarding the catalyst active site can be found: (1) active species include Na-O-Mn and Na-O-W species [19,20] and (2) active species are composed of tetrahedral WO_4 species with one W=O and three W–O–Si surface bonds [21,22]. The second theory was later revisited and it was suggested that the OCM reaction can be described with the two-metal site redox model, where the oxygen is activated on the Mn^{3+}/Mn^{2+} site and the methane is activated on the W^{6+}/W^{5+} or W^{4+} site [23]. More recently, Fleischer *et al.* performed chemical looping experiments with this catalyst and suggested a multilayer redox mechanism where the Mn provides the oxygen (oxygen storage) and tungstate contributes to activity enhancement of selective methane activation [24,25].

The strong interaction between metal oxides and the silica support was investigated by Jiang *et al.* [18]; the transformation of amorphous silica to the crystalline α-cristobalite phase was found to be directly related to the presence of Na_2WO_4. More specifically, the addition of 1 wt. % Na_2WO_4 led to the formation of cristobalite and complete transformation of amorphous silica was achieved when 4 wt. % Na_2WO_4 was used. It was later suggested by Palermo *et al.* that Na has a dual role; it acts both as a structural (by inducing the phase transformation of amorphous silica to α-cristobalite) and as a chemical promoter (by dispersing the W surface species) [26]. Long-term stability tests of the $Mn-Na_2WO_4/SiO_2$ showed that although the support material (cristobalite) gradually converted to tridymite and α-quartz phases during the OCM reaction its activity was not affected by this transition [27–30]. The only change in catalyst performance was related to the catalyst selectivity; the CO selectivity was gradually increased with a simultaneous decrease in C_{2+} selectivity over time . The decline in catalyst performance was most likely caused by the loss of active components during the reaction, as the XRD diffraction patterns collected after the 500 h stability test showed no presence of crystalline Na_2WO_4 or Mn_2O_3 phases. As shown by Wang *et al.* the W species contribute to the stability of the catalyst and the high selectivity to C_2 molecules is achieved in the presence of Na [24]. However, the catalyst characterisation for the long-term stability studies was performed *ex situ* so it is not possible to decouple the effect on the catalyst performance of the SiO_2 transformation and the loss of active components.

There are only a few studies available where the effects of promoting the Mn-Na-W/SiO_2 catalyst with La have been investigated [31–34]. Wu *et al.* were the first to study the La-Na-W/SiO_2 catalysts and it was shown that the catalytic performance is significantly enhanced when compared to the La-free catalyst (i.e. approximately 25 % C_2 yield - 25 % increase compared to the unpromoted catalyst) regardless of the amount of La loading (i.e. 0.05, 0.25, 2 and 10 wt. % La) [28]. Ghose et al. achieved 27 % C_2 yield, one of the highest reported values for fixed bed reactors in literature, using a 5 % La-10 % Na_2WO_4-5 % Mn/SiO_2 catalyst [32]. More importantly, the presence of La was shown to provide a higher performance of Mn-Na-W/SiO_2 catalyst in the OCM reaction as well as improve its stability [32,33]. However, it is still not clear how the La promoter leads to this enhancement in catalyst performance.

Over the past decade, the numerous developments of *in situ* and *operando* characterisation techniques have provided the scientific community new tools that can be employed to advance our understanding of the complex structure-activity relationships in real working catalysts and functional materials [35-45]. More importantly, the spatially-resolved spectroscopic/scattering signals collected with the tomographic approach allow us to investigate the interior of an intact device, reactor or catalyst in its industrial form and under relevant operating conditions [46-66]. As an example, we recently employed the X-ray diffraction computed tomography (XRD-CT) technique to study a La-Sr/CaO working catalyst during the OCM reaction and were able to relate the axial and radial gradients in solid-state chemistry to the imposed operating conditions [67,68]. More specifically, spatio-temporal temperature and chemical observed gradients (related to the partial pressure of CO_2) were related to the changes in the Sr-containing species: SrO-$SrCO_3$ (rhombohedral)-$SrCO_3$ (orthorhombic). We also performed the first *in* situ characterisation of a working catalytic membrane reactor. This integrated reactor system consisted of $BaCo_{0.4}Fe_{0.4}Zr_{0.2}O_{3-\delta}$ dense ceramic hollow fibre membrane and a Na-Mn-W/SiO_2 catalyst bed [69]. It was shown that the catalyst material chemically interacted with the membrane material, forming a layer of $BaWO_4$ at the inner side of the membrane. Although no significant change in reactor performance was observed during the *operando* measurements, the formation and continuous growth of the chemically stable $BaWO_4$ layer was identified as a potential barrier to the long-term stability of this system.

In this work, we employ multi-modal synchrotron chemical tomographic techniques to study a Mn-Na-W/SiO_2 and a La-promoted Mn-Na-W/SiO_2 catalyst during the oxidative coupling of methane reaction at multiple length scales. The catalysts were investigated at both the reactor level (mm scale) and single catalyst particle level (µm scale). These *operando* spatially-resolved experiments allowed us to capture these catalysts in their real active state and gain a deeper understanding of the La promoting effects.

Experimental

Catalyst preparation

The 2 wt. % La – 2 wt. % Mn – 1.6 wt. % Na – 3.1 wt. %W/SiO_2 and the 2 wt. % Mn – 1.6 wt. % Na – 3.1 wt. % W/SiO_2 catalysts were prepared by the sequential incipient wetness impregnation method (two steps process). At first a SiO_2 support (commercial Silica gel Davisil 646) was impregnated by an aqueous solution of sodium tungstate dehydrate $Na_2WO_4{\cdot}2H_2O$ and sodium oxalate $Na_2C_2O_4$ taken in appropriate amounts. The Na-W/SiO_2 was dried at 120 °C for 6 h and was then impregnated by an aqueous solution of manganese (II) acetate tetrahydrate $Mn(CH_3COO)_2{\cdot}4H_2O$ and lanthanum nitrate hexahydrate $La(NO_3)_3{\cdot}6H_2O$ salts (i.e. for the La-promoted catalyst), taken in appropriate concentrations. The catalysts were then dried at 120 °C for 6 h and calcined in air at 850 °C for 6 h with a heating rate of 2 °C min^{-1}. Each catalyst sample was sieved obtaining a size fraction of 250-500 µm.

XRD-CT measurements at ID15, ESRF

XRD-CT measurements were performed at beamline station ID15A of the ESRF using a 92.8 keV monochromatic X-ray beam focused to a spot of 25 µm x 25 µm [70]. 2D powder diffraction patterns were collected using a Pilatus3 X CdTe 300K (487 × 619 pixels, pixel size of 172 μm) hybrid photon counting area detector which uses cadmium telluride (CdTe) as the semiconducting direct conversion layer. The acquisition time per point was 50 ms. The tomographic measurements were made with 180 translation steps covering 0 - 180° angular range, in steps of 1.5° (i.e. 120 line scans). In total, 21,600 2D powder diffraction patterns were collected for each XRD-CT scan [71]. The collection of each XRD-CT dataset lasted ca. 25 min. The calibration was performed using a CeO_2 NIST standard. Every 2D diffraction image was converted to a 1D powder diffraction pattern after applying a 10 % trimmed mean filter to remove outliers or single-crystal diffraction artefacts using in-house developed MATLAB scripts [72]. The data were then reshaped to form a 3D matrix (i.e. 180 × 120 × 1500 matrix) where the 1st dimension corresponds to the translation steps, the 2nd dimension to the rotation steps and the 3rd dimension to the channels in the 1D powder diffraction patterns. Each sinogram (in total 1500 sinograms) was reconstructed using the SART algorithm from the ASTRA Toolbox [73]. In order to decrease the required computational time to reconstruct the data, the image obtained using the filtered back projection algorithm was used as the matrix for the first iteration of the SART algorithm (instead of an empty matrix). Each sinogram was reconstructed independently and the reconstructed data yielded a 180 × 180 × 1500 matrix).

The two fixed bed reactors tested comprised 2 % Mn-1.6 % Na-3.1 % W/SiO_2 and 2 % La-2 % Mn-1.6 % Na-3.1 % W/SiO_2 catalysts respectively (within 4 mm outer diameter and 2.5 mm inner diameter quartz capillary fixed bed reactors supported by glass wool). In both cases the catalyst loading was ca. 35 mg and the catalyst bed length was ca. 1 cm long. The reactor was mounted into a gas delivery stub, itself mounted to a standard goniometer (to enable alignment). The goniometer was fixed to a rotation stage set upon a translation stage to facilitate the movements required for the CT measurements. Dry air and pure gases CH_4 and He were delivered to the reactor by GF40 Brooks mass flow controllers. Heating was achieved by virtue of two hot air blowers (Cyberstar) heating each side of the catalytic reactor to ensure homogeneous temperature distribution over the catalyst bed [74]. The hot air blowers were mounted on the translation stage and were moving with the reactor during the translation scans, maintaining the hot air blowers-to-reactor distance constant. XRD-CT measurements were performed at nominal temperatures, ambient up to 1000 °C equating to actual temperatures (i.e. after temperature calibration) of ambient and 800 °C with a nominal ramp rate of 5 °C min^{-1}. During the XRD-CT measurements, the outflow gasses were monitored by mass spectrometry using an Ecosys portable mass spectrometer. The mass spec line was inserted inside the capillary from the top. The experimental setup and temperature calibration are shown in Figures S1 and S2 in the Supporting Information.

Multimodal μ-XRF/XRD/absorption-CT measurements at I18, DLS

Combined μ-XRF-CT and μ-XRD-CT measurements were performed at beamline station I18 of the Diamond Light Source using a 13 keV monochromatic X-ray beam with a spot size of 2.3 μm (V) × 3.5 μm (H). XRF spectra were collected with the four element Standard Vortex Si Drifts detector (2 -15 keV). 2D powder diffraction patterns and XRF spectra were collected at 5 μm intervals with a collection time of ca. 350 ms per point. Each XRD-CT scan lasted ca. 100 min. The 2D powder diffraction patterns were recorded with a Photonic Sciences CMOS-based X-ray imaging detector. The calibration was performed using a LaB_6 reference material. Catalyst particles were placed inside open-ended quartz capillaries of 0.5 mm outer diameter and 0.05 mm wall thickness, supported by glass wool. Typically, a total of 125 translation steps were performed for each tomographic angle and in total 55 angles were used. The angular step size was 3.5 ° and the angular range covered was 0-189 °. This was necessary due to the complex experimental setup, shown in Figure S3 in the Supporting Information. During the tomographic scans the quartz support rod of the reactor cell started adjacent to the IR heater, and rotated anti-clockwise, stopping just before the XRF detector at ca. 200 °. This slight increase in angular scan range was because the support rod temporarily blocked the incident beam, however at no stage were the XRD or the XRF detectors were blocked. Approximately 3 rows of the sinogram could not be used, this was accounted for by the increased rotational range and did not have a detrimental effect on the reconstruction. Every 2D diffraction image was converted to a 1D powder diffraction pattern after applying a 30 % trimmed mean filter to supress the single-crystal diffraction artefacts using in-house developed MATLAB scripts [72]. The data were then reshaped to form a 3D matrix (i.e. 125 × 55 × 2200 matrix) where the 1st dimension corresponds to the translation steps, the 2nd dimension to the rotation steps and the 3rd dimension to the channels in the 1D powder diffraction patterns. Each sinogram (in total 2200 sinograms) was reconstructed using the SART algorithm from the ASTRA Toolbox. In order to decrease the required computational time to reconstruct the data, the image obtained using the filtered back projection algorithm was used as the matrix for the first iteration of the SART algorithm (instead of an empty matrix). Each sinogram was reconstructed independently and the reconstructed data yielded a 125 × 125 × 2200 matrix).

The temperature of the reactors was controlled with the Thermo Riko's GA198 - 1kW Atmospheric Quartz guided Infrared (IR) heater. The IR heater was placed on a motorised stage in order to maintain the sample to IR heater distance constant during the tomographic measurements. The IR heater was positioned within 2.0 mm of the sample and it was operated at the maximum stable temperature to ensure maximum heating. Prior to the beamtime experiment, temperature calibration experiments were performed to ensure that the operating temperature of 800 °C can be reached with this heating system. The combined μ-XRF-CT and μ-XRD-CT measurements were made at room temperature, under OCM reaction conditions (ca. 800 °C) and at room temperature at the end of the each experiment. A reaction mixture of 50 % vol. CH_4/Ar and 20 % vol. O_2/He was used keeping the CH_4/O_2 molar ratio equal to 4 in both experiments (i.e. 6 ml min^{-1} of 50 % vol. CH_4/Ar and 3.75 ml min^{-1} of 20 % vol. O_2/He were used). The flow of gases was monitored/controlled with Brooks GF40 mass flow controllers and the gas products were analysed with an Omnistar portable mass spectrometer.

High temperature and PXRD measurements

The powder diffraction measurements were performed in Bragg-Brentano geometry with a Rigaku Smartlab diffractometer (Cu $K_{\alpha 1}$ radiation wavelength 0.154 nm) using a D/tex Ultra 250 1D silicon strip detector and a 2-bounce Ge monochromator (220) in parallel beam geometry. An Anton Parr HTK hot stage was used for the measurements from ambient temperature to 800 °C under He flow (30 ml min^{-1}). The angular range covered was 10-90 °2θ with a step size of 0.01 ° (acquisition speed of 0.7 ° min^{-1}). The temperature ramping rate was 10 °C min^{-1} and a time period of 10 min was allowed for temperature stabilisation before the acquisition of each powder diffraction pattern.

Rietveld analysis of XRD-CT data

Quantitative Rietveld refinement was performed using the reconstructed diffraction patterns, on a voxel by voxel basis. The MultiRef MATLAB framework was chosen for the Rietveld analysis as MATLAB allows for parallel computing using multicore processors. Such a feature is essential when full powder profile analysis of XRD-CT data is attempted due to the very large number of datasets. The Multiref framework reads/writes the required files and the Rietveld refinement is performed by the GSAS software [75]. The results from the refinements can be imported into MALTAB and create the various images (e.g. phase distribution maps based on the scale factors, lattice parameters etc.). The strategy applied for the Rietveld analysis of the collected XRD-CT data is presented in the Supporting Information (Sections 2 and 3). The Rietveld refinement analysis of the XRD-CT data presented herein was based on the intensity of the scale factors and as such it is treated as a semi-quantitative analysis. In order to have a good starting model, the summed diffraction pattern of each XRD-CT dataset (i.e. reconstructed data volume) was exported and then quantitative Rietveld analysis was performed.

Results and discussion

XRD-CT experiments during OCM – unpromoted Mn-Na-W/SiO_2 catalyst

A schematic representation of the experimental protocol followed for the OCM experiment with the 2 % Mn-1.6 % Na-3.1 % W/SiO_2 catalyst is shown in Figure S6 (more detailed information about the experimental condition can be found in Table S1). Initially, an XRD-CT scan (1) of the fresh catalyst was collected at room temperature. The temperature of the reactor was then increased to 800 °C with a ramp rate of 5 °C min^{-1} under the flow of He (i.e. 30 ml min^{-1}). Four interlaced XRD-CT (IXRD-CT) scans were collected during temperature ramping (2-5) [71]. Once the required temperature was reached, another XRD-CT scan was performed (6). The inlet gas was then switched to air (i.e. 50 ml min^{-1}) and an XRD-CT scan was collected (7) as it has been previously suggested that high temperature pre-treatment under air can yield a catalyst with better performance [76]. The catalyst bed was then exposed to various OCM reaction gas mixtures (i.e. gas mixtures of CH_4/He/Air). Since there is a lot of debate in literature regarding the long-term stability and reasons behind the deactivation of this family of catalysts (i.e. Mn-Na-W/SiO_2 catalysts), it was considered essential to investigate the behaviour of the catalyst under CH_4 rich environments (i.e. very reducing environments). The inlet gas mixture was switched to CH_4 / Air with a molar ratio of 10:1 (total flow rate of 110 ml min^{-1}) and an XRD-CT scan was performed (8). This gas mixture was maintained during cooling to room temperature, till the end of the experiment. The final XRD-CT scan was performed at room temperature after the OCM experiment (11). The phase identification of the fresh 2 % Mn-1.6 % Na-3.1 % W/SiO_2 catalyst was performed using the summed diffraction pattern from a room temperature XRD-CT scan before the OCM experiment. The crystalline phases identified were: Cristobalite-low, Tridymite-low, Quartz-low, Na_2WO_4, Mn_2O_3 and/or $MnMn_6SiO_{12}$.The results of the phase identification are presented in Figure 1, where a region of interest of the summed diffraction pattern is shown. The crystallographic details regarding the identified phases can be found in the Supporting Information (Table S2).

It should also be noted here that, as previously stated in literature, it is very challenging to reach a conclusion whether the Mn_2O_3 (Bixbyite) or the Mn_7SiO_{12} (Braunite) or both phases are present in the Mn-W-Na/SiO_2 catalysts[77,78]. The highest intensity peak generated by these phases is at approximately Q = 2.31 Å^{-1} ((222) reflection for Mn_2O_3 and (224) reflection for Mn_7SiO_{12}). However, as it is clearly shown in Figure 1, this is a minor peak even when the summed diffraction pattern is used (small peak at the right side of a Na_2WO_4 peak). As these two phases generate very similar diffraction patterns and mainly one diffraction peak can be observed, the Rietveld analysis of the XRD-CT data was performed using only the Mn_2O_3 structure in the model (higher symmetry).

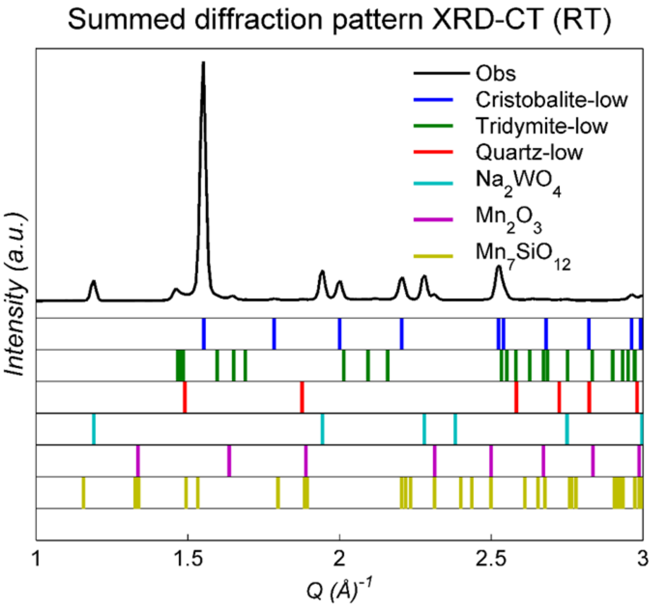

Figure 1: Phase identification of the 2 % Mn-1.6 % Na-3.1 % W/SiO_2 catalyst. Black line: the summed diffraction patterns from the room temperature XRD-CT scan (i.e. after applying a binary mask to the reconstructed data in order to extract the diffraction patterns generated only by the sample), Blue ticks: Cristobalite, Green ticks: Tridymite, Red ticks: Quartz, Cyan ticks: Na_2WO_4, Magenta ticks: Mn_2O_3, Yellow ticks: Mn_7SiO_{12}.

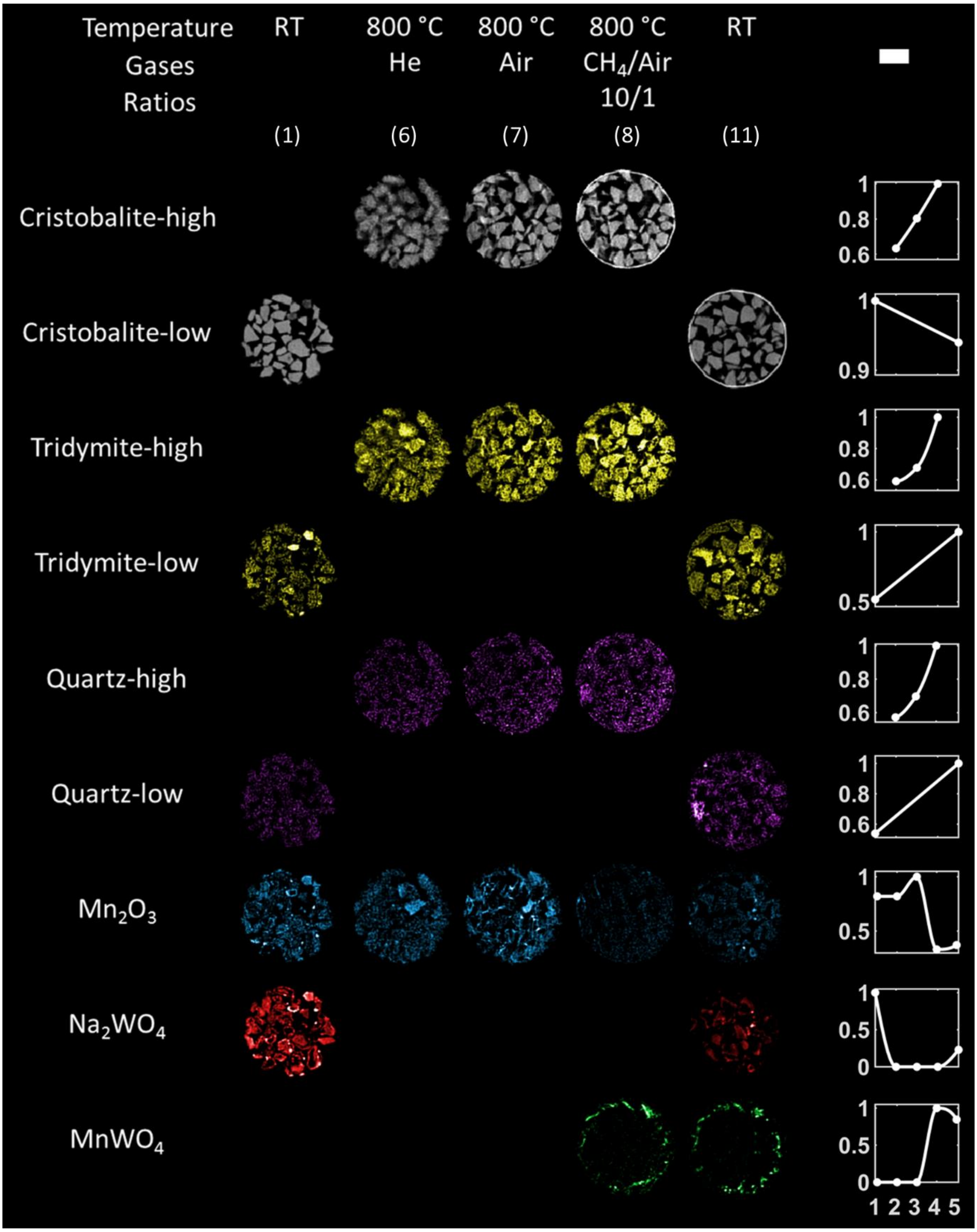

Figure 2: Phase distribution maps created based on the intensities of the scale factors of each crystalline phase. Right: Relative changes of each component during the OCM experiment with the Mn – Na – W/SiO₂ catalyst (operating conditions 1 to 5). Scale bar corresponds to 0.75 mm.

These phase distribution maps represent the values of the scale factors of each crystalline phase (XRD-CT scans 1, 6, 7, 8 and 11, see also Figure S6). The summed intensity of the scale factors over each XRD-CT scan was calculated and these values were then normalised with respect to the maximum value. These results are plotted at the right side of Figure 2 and show the relative change of each crystalline phase during the OCM experiment.

Looking at the results obtained from the fresh 2 % Mn-1.6 % Na-3.1 % W/SiO_2 catalyst (i.e. room temperature XRD-CT scan), it can be seen there a few catalyst particles rich in tridymite but, in general, it is the cristobalite phase distribution map that describes very well the catalyst particles in terms of both shape and size. As shown previously, in the summed diffraction pattern presented in Figure 1, there are only minor amounts of quartz in the fresh catalyst. The $NaWO_4$ and the Mn_2O_3 / Mn_7SiO_{12} phases are not perfectly co-located which is to be expected as the catalyst was prepared by the sequential incipient wetness impregnation method (Figure S7).

Upon reaching the required high temperatures for the OCM reaction, the crystalline Na_2WO_4 phase has disappeared. The cubic Na_2WO_4 first transforms into a lower symmetry orthorhombic Na_2WO_4 phase and then this new phase disappears too (Figure S8). At 800 °C, no Na-W-O phase is observed in the XRD-CT data. During temperature ramping to 800 °C, there was sample movement and as a result the data acquired from XRD-CT scan 6 yielded blurred images. As it will be shown in the following section, this sample movement was a result of a chemical interaction of the catalyst with the capillary and not of just thermal expansion of the sample. The phase identification of the 2 % Mn-1.6 % Na-3.1 % W/SiO_2 catalyst at 800 °C (He flow) was performed using the summed diffraction pattern (XRD-CT dataset 6). The results from the phase identification are presented in Figure S9, where a region of interest of the summed diffraction pattern is shown.

The sample stabilized with time at 800 °C. However, the subsequent XRD-CT scans (i.e. XRD-CT scans 7 and 8) were collected at a different height (i.e. vertical position) of the catalyst bed compared to XRD-CT scan 6 due to the sample movement. This means that the result obtained from the Rietveld analysis showing the crystalline Mn_2O_3 / Mn_7SiO_{12} phases growing during the activation step (i.e. air flow of 50 ml min^{-1}) should be treated with caution. On the other hand, there are significant solid-state changes taking place under reducing conditions (XRD-CT scan 8). At this point it should be noted that five different reaction mixtures were introduced to the catalyst bed prior to XRD-CT scan 8 in order to validate that the reactor was active for the OCM reaction. The reaction mixtures used for the OCM experiment are shown in Table S3.

The introduced OCM reaction conditions induced important solid-state changes; the diffraction signal generated by the Mn_2O_3 / Mn_7SiO_{12} phases is seen to be diminished while a new crystalline Mn phase identified as $MnWO_4$ is formed [77]. This result shows that under very reducing environments (i.e. CH_4 : Air = 10:1), not only the surface Mn^{3+} species reduce to Mn^{2+} species but also the bulk ones do too. The formation of $MnWO_4$ after an OCM experiment has been previously observed from powder diffraction measurements [79–81]. However, to our knowledge, this is the first true *operando* experiment of this family of catalysts. As shown with the mass spectrometry data collected during the XRD-CT scan 8 (Figure S10) there is no change in the mass spectrometry signals during the collection of the XRD-CT scan (no deactivation is implied due to the formation of $MnWO_4$), it is now evident that crystalline Mn_2O_3 / Mn_7SiO_{12} is not required for an active OCM catalyst.

More importantly, the spatially-resolved experiments performed with the XRD-CT technique have revealed new information; information that is otherwise lost in bulk measurements. As shown clearly in the phase distribution map of $MnWO_4$, in Figure 2, this new phase is not homogeneously distributed over the catalyst bed. On the contrary, the distribution of the $MnWO_4$ phase is highly heterogeneous as it is seen to preferentially grow close to the capillary wall (but not at it). Additionally, the formation of a crystalline cristobalite ring is observed. It is evident that the crystallization of the amorphous SiO_2 capillary took place at 800 °C. However, as in the case of the Mn-Na-W/SiO_2 catalysts, this phenomenon is only possible at relatively lower temperatures because of the presence of Na^+ ions. It is therefore implied that the Na^+ ions are unstable in this catalyst under OCM reaction conditions and they become volatile. It has been recently shown that the WO_4^{2-} ions are mobile too (melting point of Na_2WO_4 is 698 °C) and can interact with other materials [69]. It is also crucial to point out that there are no new crystalline Mn-species formed closer to the middle of the catalyst bed (i.e. where $MnWO_4$ is absent and the signal of Mn_2O_3 / Mn_7SiO_{12} has diminished) which implies that Mn-species are present in an amorphous/nano-crystalline state. This has also been recently suggested by Sinev *et al.*; it was claimed that there are both crystalline and molten phases at the catalyst at high temperatures including Mn-species in an amorphous "glue-like matter" that contains mobile Na^+ and possibly Mn^{2+} species [82].

After cooling to room temperature at the end of the OCM experiment (Figure S11), Na_2WO_4 is seen to reform, albeit to a lesser extent. This is reasonable as the $MnWO_4$ phase is stable and is maintained until the end of the experiment. However, it can be seen in the phase distribution map of Na_2WO_4 in Figure 2 that it is mainly present closer to the center of the catalyst bed rather than to the capillary. Furthermore, the results presented in Figure 2 also suggest that there is also an evolution of the SiO_2 support at the high temperatures required for the OCM reaction. It is suggested from the Rietveld analysis that the evolution taking place is the following:

Amorphous silica → Cristobalite → Tridymite → Quartz

Although this should be treated with care due to the sample movement during the high temperature scans, it is also supported by the weight fraction maps presented in Figure S13. The solid-state evolution of SiO_2 at relatively low temperatures (800 °C) when alkali metals are present has been reported and investigated on several occasions [83–86]. Venezia *et al.* suggested that the alkali ions occupy interstitial sites, collapsing the Si-O-Si bridges and as a results leading to the formation of crystalline forms from amorphous silica [84]. The incorporation of Na species into the silica framework is implied in Figure S12 in the Supporting Information, where the maps of the lattice parameter *a* of the SiO_2 cristobalite-low phase are presented. It has also been previously shown that the transformation to various SiO_2 crystalline phases and from one crystalline phase to another, depends on the temperature, alkali species and alkali loading [84,87]. It is therefore no wonder there is an evolution of the support as a function of time at high temperatures since there are mobile and volatile Na^+ ions present in this catalyst.

XRD-CT experiments during OCM – La promoted Mn-Na-W/SiO_2 catalyst

As it will be shown in this section, the solid-state chemistry taking place in the 2 % La-2 % Mn-1.6 % Na-3.1 % W/SiO_2 catalyst is significantly different compared to the unpromoted 2 % Mn-1.6 % Na-3.1 % W/SiO_2 catalyst. A schematic representation of the experimental protocol followed for the OCM experiment with the 2 % La-2 % Mn-1.6 % Na-3.1 % W/SiO_2 catalyst is shown in Figure S16. Initially, an XRD-CT scan (1) of the fresh catalyst was collected at room temperature. The temperature of the reactor was then increased to 800 °C with a ramp rate of 5 °C min^{-1} under the flow of He (i.e. 30 ml min^{-1}). Four IXRD-CT scans were collected during temperature ramping (2-5). Once the required temperature was reached, two XRD-CT scans were performed (6-7). The inlet gas was then switched to air (i.e. 50 ml min^{-1}) and an XRD-CT scan was collected (8). After this activation step, the catalyst bed was exposed to various OCM reaction gas mixtures (i.e. gas mixtures of CH_4/He/Air) and three XRD-CT scans were performed (9-11). Two IXRD-CT scans were collected during cooling (12-13) and a final XRD-CT scan was performed at room temperature after the OCM experiment (14).

The phase identification of the fresh 2 % La-2 % Mn-1.6 % Na-3.1 % W/SiO_2 catalyst was performed using the summed diffraction pattern from the room temperature XRD-CT scan (Figure 3). The crystalline phases identified were: Cristobalite-low, Tridymite-low, Quartz-low, Na_2WO_4, Mn_2O_3 and/or $MnMn_6SiO_{12}$. The only crystalline La-containing phase identified was $La_4Mn_5Si_4O_{22}$ (Figure S17). The crystallographic details regarding the identified phases can be found in the Supporting Information (Table S4). In a previous study of this catalyst, TEM/EDX analysis suggested the presence of the La-containing phase although it was not observed with traditional powder XRD [32]. Here, with XRD-CT measurements we are able to identify a La-Mn-O phase, which is a direct evidence that La directly interacts with both the support and the Mn species.

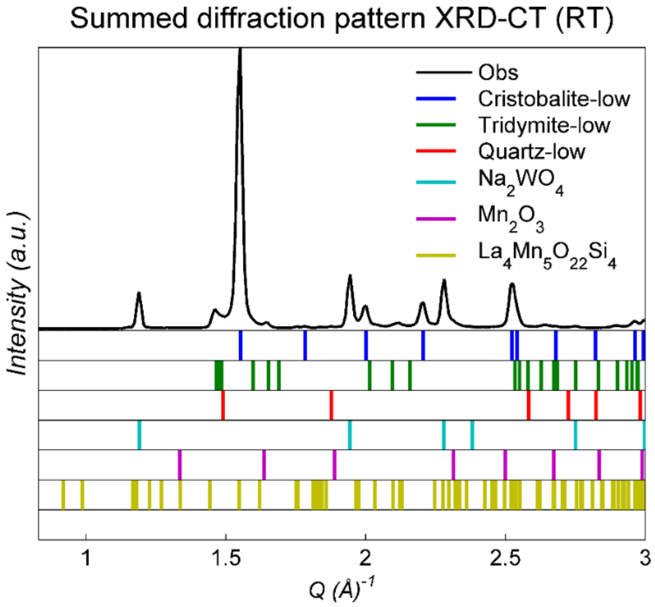

Figure 3: Phase identification of the 2 % La-2 % Mn-1.6 % Na-3.1 % W/SiO_2 *catalyst. Black line: the summed diffraction pattern from the room temperature XRD-CT scan (i.e. after applying a binary mask to the reconstructed data in order to extract the diffraction patterns generated only by the sample), Blue ticks: Cristobalite, Green ticks: Tridymite, Red ticks: Quartz, Cyan ticks:* Na_2WO_4*, Magenta ticks:* Mn_2O_3*, Yellow ticks:* $La_4Mn_5Si_4O_{22}$*.*

The results from the Rietveld analysis of the XRD-CT data collected during the OCM experiment with the 2 % La-2 % Mn-1.6 % Na-3.1 % W/SiO_2 catalyst are presented in Figure 4. As in the case of the 2 % Mn-1.6 % Na-3.1 % W/SiO_2 catalyst, these phase distribution maps represent the values of the scale factors of each crystalline phase (XRD-CT scans 1, 6-12 and 14, see also Figure S16). The summed intensity of the scale factors over each XRD-CT scan was normalised with respect to the maximum value. The results are plotted at the right side of Figure 4 and show the relative change of each crystalline phase during the OCM experiment.

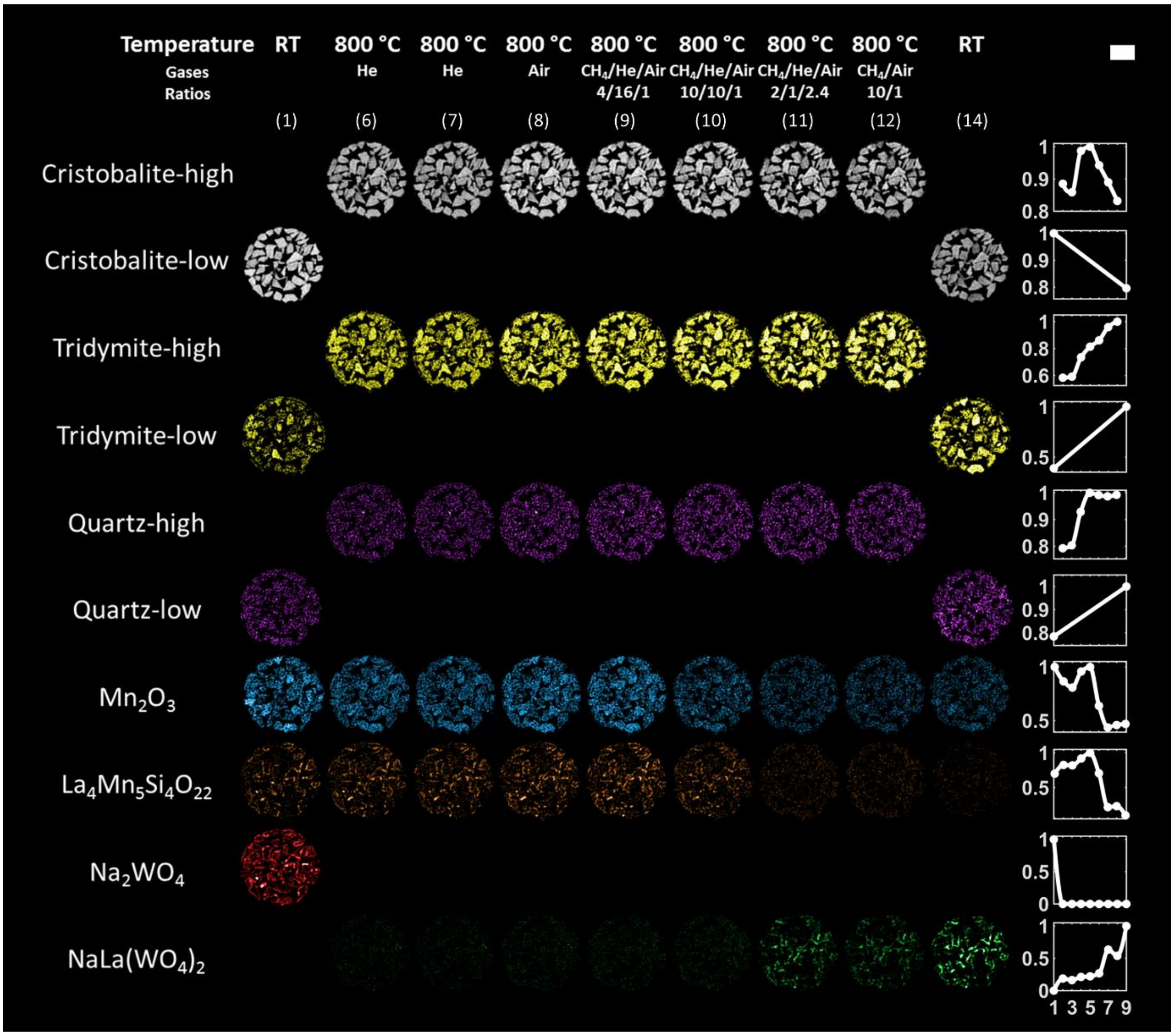

Figure 4: Phase distribution maps created based on the intensities of the scale factors of each crystalline phase. Right: Relative changes of each component during the OCM experiment with the La-Mn-Na-W/SiO$_2$ catalyst (operating conditions 1 to 9). Scale bar corresponds to 0.75 mm.

As shown in Figure 4 and in contrast to the phase distribution map of Na$_2$WO$_4$ of the fresh 2 % Mn-1.6 % Na-3.1 % W/SiO$_2$ catalyst (Figure 2), the majority of the Na$_2$WO$_4$ phase present in the La-promoted catalyst is located near/at the surface of the catalyst particles. This is also the case for the La$_4$Mn$_5$Si$_4$O$_{22}$ phase. On the other hand, the phase distribution map of Mn$_2$O$_3$ / Mn$_7$SiO$_{12}$ shows that it is homogeneously distributed over the catalyst particles which indicates that the presence of La enhances the dispersion of Mn species.

Once the required temperature was reached (800 °C), an XRD-CT scan (i.e. XRD-CT scan 6) was performed. However, due to a beam refill during the acquisition of this XRD-CT scan it was decided to acquire a second XRD-CT prior to switching from He to air flow (i.e. XRD-CT scan 7). As there were no solid-state changes during these two XRD-CT scans collected under

He flow (i.e. XRD-CT scans 6 and 7), only the results from the second XRD-CT are presented in Figure 4. This is reasonable as the total acquisition time for the two XRD-CT scans was approximately 1h 30min; a relatively short period of time for substantial changes to take place in an inert chemical environment. The next XRD-CT scan (XRD-CT scan 8) was acquired while air flowed through the catalyst bed (50 ml min^{-1}). In Figure 4, it is implied that the diffraction signal from both the Mn_2O_3 / Mn_7SiO_{12} and the $La_4Mn_5Si_4O_{22}$ phases slightly increased. However, the signal generated by these phases significantly decreased once the first CH_4/He/air reaction mixture was used. The four reaction mixtures used in the OCM experiment with the La-promoted catalyst are provided in Table S5.

It is clearly shown in Figure 4 that the diffraction signal from the Mn_2O_3 / Mn_7SiO_{12} and the $La_4Mn_5Si_4O_{22}$ phases ($La_4Mn_5Si_4O_{22}$ has completely disappeared by the end of the OCM experiment) decreased radically when the OCM reaction mixture 2 was used (i.e. CH_4:Air = 10:1). This is expected as the metals in the various metal oxides present in the catalyst will eventually be reduced under these conditions. However, it can be also clearly seen that there are significant differences compared to the La-free catalyst. More specifically, the Mn_2O_3 / Mn_7SiO_{12} signal diminished in the 2 % Mn-1.6 % Na-3.1 % W/SiO_2 catalyst under the same operating conditions (i.e. CH_4:Air = 10:1). As mentioned previously, the Mn species were reduced and a $MnWO_4$ phase formed. However, in the case of the La-promoted catalyst, the Mn_2O_3 / Mn_7SiO_{12} phases were present for the duration of the whole OCM experiment.

The significance of this result is more apparent when it is taken into account the fact that the La-promoted catalyst was exposed to reducing environments for more than double the time compared to the unpromoted catalyst (ca. 3.5 h for the 2 % La-2 % Mn-1.6 % Na-3.1 % W/SiO_2 catalyst to 1.5 h for the 2 % Mn-1.6 % Na-3.1 % W/SiO_2 catalyst). This result suggests that the La acts as a chemical promoter leading to more stable and difficult-to-reduce Mn species. Furthermore, a new crystalline phase, identified as $NaLa(WO_4)_2$ formed at high temperatures. The results from the phase identification performed using the summed diffraction pattern from the XRD-CT scan collected at room temperature after the OCM experiment is shown in Figure S20. This means that the most important role of La is to stabilise the mobile and volatile Na^+ and WO_4^{2-} species by leading to the formation of this new crystalline phase which is seen to be stable and present until the end of the OCM experiment. As shown in Figure S21, in contrast to the La-free catalyst, there is no crystalline Na_2WO_4 present after cooling to room temperature at the end of the OCM experiment. This proves that the La works efficiently as a trap of the mobile/volatile species present in the catalyst at high temperatures. Further to this, it seems also that La plays a role in supressing the onset of deleterious support changes (Figure 4). Cristobalite is seen again to transform to tridymite at high temperatures as a function of time but the formation and growth of quartz is suppressed. This result was also later verified with *ex situ* PXRD characterisation of the two catalyst (see the section High temperature PXRD). Micro-CT images of both catalysts collected before and after OCM are presented in Figures S19 and S20 providing further evidence for the instability of the unpromoted catalyst.

Multimodal μ-XRF/XRD/absorption-CT experiments during OCM

In this section the results from the OCM experiments, with combined μ-XRF/XRD/absorption-CT, of the 2 % Mn-1.6 % Na-3.1 % W/SiO_2 catalyst and the 2 % La-2 % Mn-1.6 % Na-3.1 % W/SiO_2 catalysts are presented. The purpose of these experiments was to investigate the evolution of these catalysts under OCM conditions at a different length scale (i.e. single catalyst particle level). This means that the results obtained from these experiments serve to complement the XRD-CT experiments presented in the previous section, leading to a true multi-length-scale investigation of these systems (i.e. from the reactor to the single catalyst particle level).

The 2 % Mn-1.6 % Na-3.1 % W/SiO_2 catalyst

μ-XRF-CT

The results from the μ-XRF-CT/ μ-absorption-CT scans of the 2 % Mn-1.6 % Na-3.1 % W/SiO_2 catalyst are presented in Figure 5. The μ-XRF-CT scan of the fresh catalyst (i.e. at room temperature) revealed that the W and Mn species are not perfectly co-located in the catalyst particles. This result is in good agreement with the results obtained from the XRD-CT data presented in the previous section (Figure 2).

The high temperature μ-XRF-CT scans were performed at four different vertical positions (Pos 1 to 4 in Figure 5). As it is clearly implied from the μ-absorption-CT maps in Figure 5, different catalyst particles were probed during the tomographic scans at high temperatures compared to the room temperature scans. This is attributed to the thermal expansion of the capillary and not to sample movement as the tomographic scans performed at room temperature before and after the OCM experiment probed the same catalyst particles.

The high temperature μ-XRF-CT scans (ca. 800 °C) revealed new information about this catalyst. The results shown in Figure 5 imply that the Na_2WO_4 phase does not just melt at high temperatures but it also becomes volatile. This is in full agreement with the results from the XRD-CT experiments of the same catalyst presented in the previous section. However, the results obtained from the μ-XRF-CT scans clearly show that the W containing species also migrate from the catalyst particles to the inner capillary wall. A very thin layer of W containing species is seen to form and grow as a function of time at high temperatures. This "coating" phenomenon is irreversible and this new layer is present even after cooling to room temperature. This W layer was not observed with the XRD-CT data (neither with ID15A nor with the I18 XRD-CT data) which implies it is not highly crystalline. It is reminded though that the gaseous chemical environment can have an impact on the W "coating" phenomenon. For example, it was previously shown that highly reducing conditions can lead to the formation of $MnWO_4$ through the interaction of the partially reduced Mn species with the mobile WO_4^{2-} species. In that case, the "coating" phenomenon is prevented but the loss of W-containing species, which are considered to be part of the active catalyst, is not.

It is important to note here that the W XRF signal seems to be dominated by the W species present at the new layer to such an extent that the W species present in the catalyst particles are barely visible in the XRF-CT maps. The migration and volatility of W containing species was also suggested from the *ex situ* SEM/WDS images (elemental map of W) presented in Figures S21 and S22 in the Supporting Information. On the other hand, the Mn species are seen to be more stable (i.e. no apparent migration from the catalyst particles to the inner capillary wall).

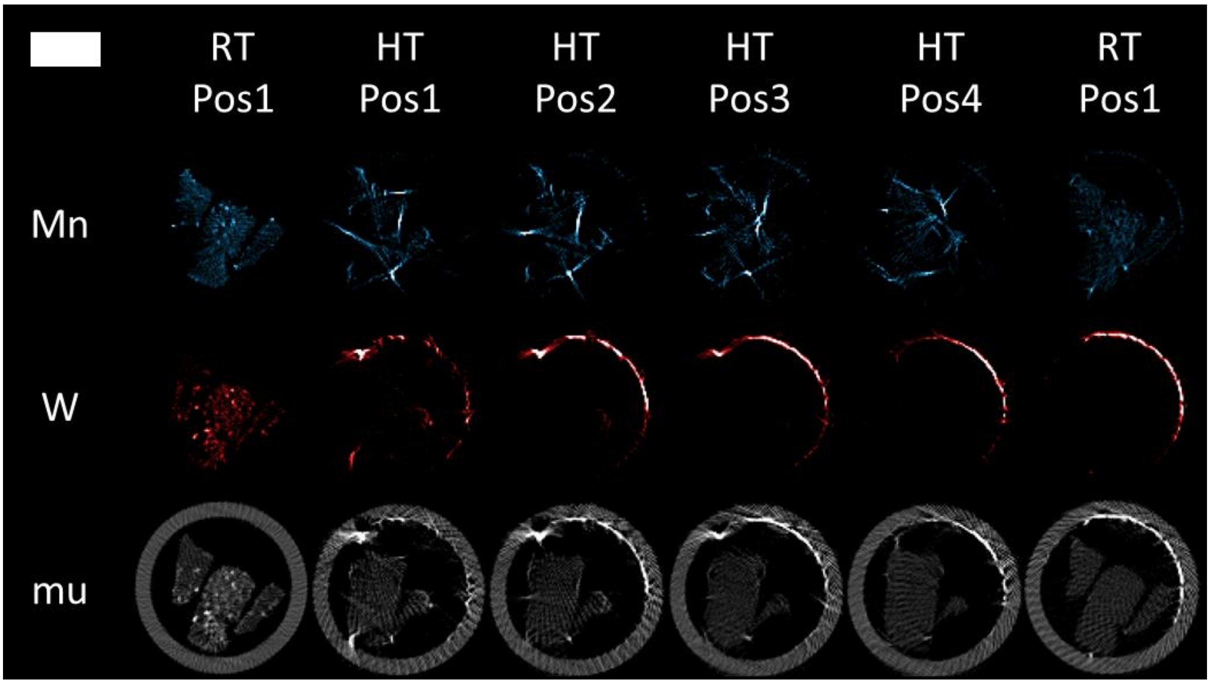

Figure 5: Elemental maps of Mn, W and μ-absorption-CT map (mu) of the 2 % Mn-1.6 % Na-3.1 % W/SiO$_2$ catalyst – RT for room temperature scans, HT for high temperature scans (ca. 800 °C). The high temperature μ-XRF-CT scans were performed at four different vertical positions (Pos 1 to 4). Scale bar corresponds to 0.25 mm.

μ-XRD-CT

The 2D powder diffraction images acquired during the μ-XRD-CT measurements exhibited spottiness due to the presence of large crystallites in the sample (i.e. large relative to the beam size). A 30% alpha-trimmed mean filter was used to remove outliers and suppress the formation of "streak" artefacts in the reconstructed images. However, as this is a relatively harsh filter and the *Q* range sampled was very narrow (ca. 1-3.4 Å^{-1}), the μ-XRD-CT data were processed by fitting specific peaks of interest (i.e. one peak per crystalline phase) rather than performing full profile Rietveld analysis. The results from the phase identification of the fresh 2 % Mn-1.6 % Na-3.1 % W/SiO$_2$ catalyst are presented in Figure S28. As expected, the same crystalline phases were identified as in the XRD-CT experiments described in the previous section (i.e. cristobalite-low, tridymite-low, Na_2WO_4 and Mn_2O_3 / Mn_7SiO_{12}).

The diffraction peaks of each crystalline phase selected for the peak fitting analysis are summarised in Table S6. A Gaussian peak shape function was used and three refinement cycles were performed allowing for three iterations in each cycle. In the first refinement cycle, the area of the peak and the background (1st degree polynomial) were refined. In the second cycle, the peak position was refined along with the previous parameters and in the final refinement cycle, the full width at half maximum (FWHM) was added to the refinement.

The results obtained from the peak fitting analysis of the μ-XRD-CT are shown in Figure 6 where the various phase distribution maps, as obtained from the integrated intensities of the respective phases, are presented. In Figure 6, it can be seen that the Na_2WO_4 and the Mn_2O_3/Mn_7SiO_{12} are not perfectly co-located in the fresh catalyst (i.e. room temperature μ-XRD-CT scan) which is in full agreement with the μ-XRF-CT results and the XRD-CT results presented in the previous section. More importantly, it is clearly shown that at high temperatures there is formation and growth of a cristobalite ring at the capillary (reactor vessel). This is important as it proves that the XRD-CT results presented in the previous section are reproducible (Figure 2).

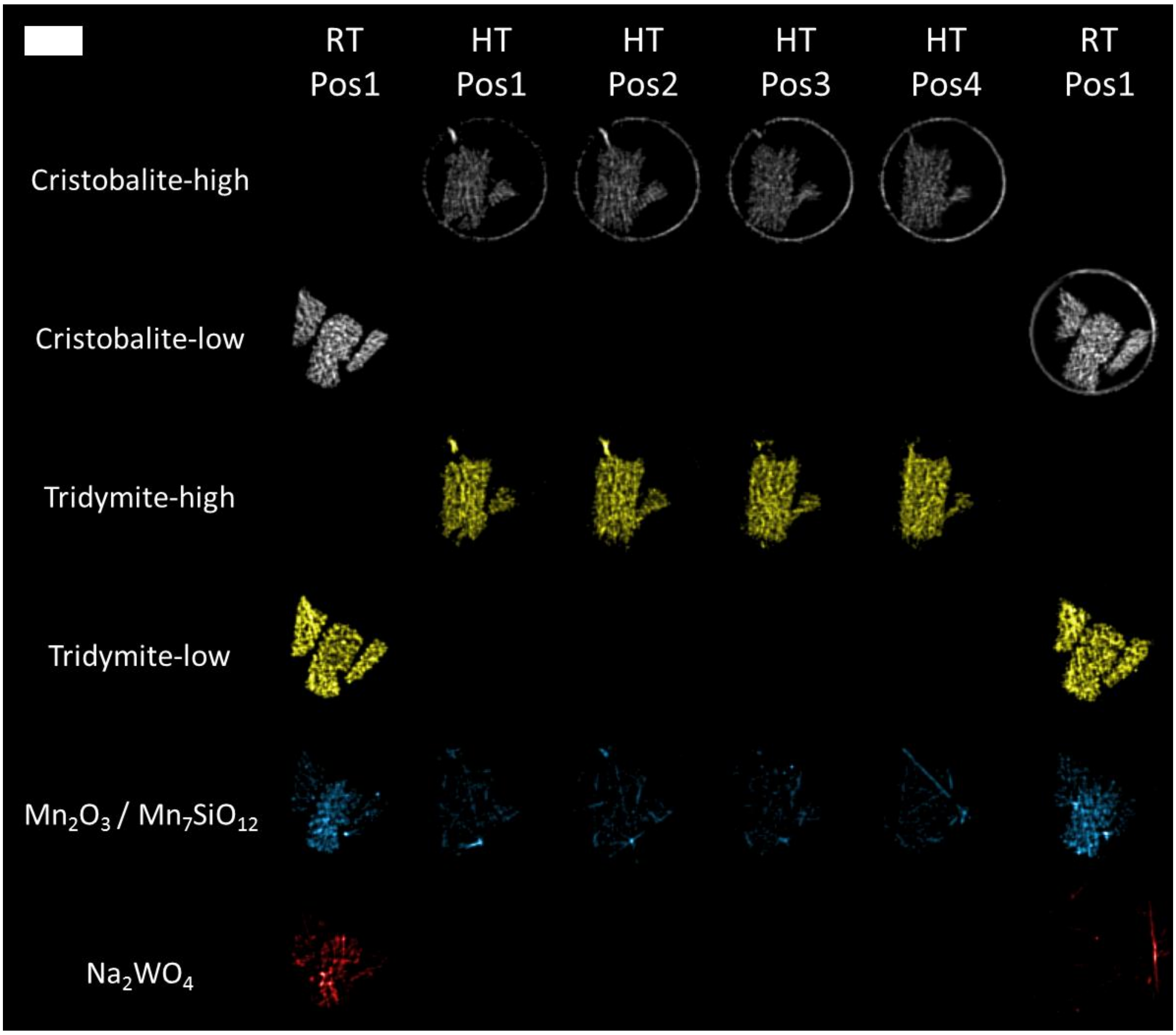

Figure 6: Phase distribution maps of the various crystalline phases present in the 2 % Mn-1.6 % Na-3.1 % W/SiO_2 catalyst during the OCM experiment. Scale car corresponds to 0.25 mm.

On the other hand, the Mn_2O_3/Mn_7SiO_{12} phases remained present for the duration of this OCM experiment and no $MnWO_4$ was observed. This observation further supports the claim made in the previous section that the formation/growth of $MnWO_4$ directly depends on the gas environment. In contrast to the previous XRD-CT experiment, where the behaviour of the 2 % Mn-1.6 % Na-3.1 % W/SiO_2 catalyst was investigated under very reducing environments, the CH_4:O_2 ratio was kept constant at 4 for the duration of this OCM experiment. As a result, the majority of the Mn species did not reduce from Mn^{3+} to Mn^{2+}, at least according to the μ-XRD-CT data (i.e. Mn_2O_3/Mn_7SiO_{12} were the only Mn crystalline phases present in the catalyst). Of course, the loss of reactive WO_4^{2-} ions from the catalyst bed to the capillary (as implied from the μ-XRF-CT data) also contributed to the prevention of the $MnWO_4$ formation.

In Figure 6, it can also be seen that the Na_2WO_4 phase reforms after cooling to room temperature at the end of the OCM experiment, but it is mainly present at the inner side of the capillary rather than the catalyst particles. The summed diffraction patterns of all the μ-XRD-CT data acquired from the 2 % Mn-1.6 % Na-3.1 % W/SiO2 catalyst are presented in Figure S30.

The 2 % La-2 % Mn-1.6 % Na-3.1 % W/SiO_2 catalyst

μ-XRF-CT

The μ-XRF-CT scans of the 2 % La-2 % Mn-1.6 % Na-3.1 % W/SiO_2 catalyst are presented in Figure 7. Three μ-XRF-CT scans were performed at 3 different vertical positions by moving the sample in the *z* direction with a step size of 5 μm (Positions 1 to 3 in Figure 7). The μ-XRF-CT scan of the fresh catalyst (i.e. at room temperature) revealed that there are regions in the sample where some elements are co-located and other regions where they are not. It should be noted that in contrast to the 2 % Mn-1.6 % Na-3.1 % W/SiO_2 catalyst, the Mn and at a lesser extent the La XRF-CT data in the 2 % La-2 % Mn-1.6 % Na-3.1 % W/SiO_2 catalyst suffer from self-absorption artefacts. This can be observed from the abnormal higher intensity at the right side of all particles. At high temperatures, it can be seen that there is again migration of the W containing species, albeit to an impressively lesser extent when compared with the 2 % Mn-1.6 % Na-3.1 % W/SiO_2 catalyst. The difference is apparent when the μ-absorption-CT maps obtained from the two experiments are directly compared (Figures 5 and 7). The Mn species are seen to be stable as there is no indication of Mn species leaving the catalytic particles. This is also true for the La-containing species. However, these two results should be treated with caution as the sample volume probed during these μ-XRF-CT scans was not the same (due to the thermal expansion of the capillary during the OCM experiment, as previously discussed).

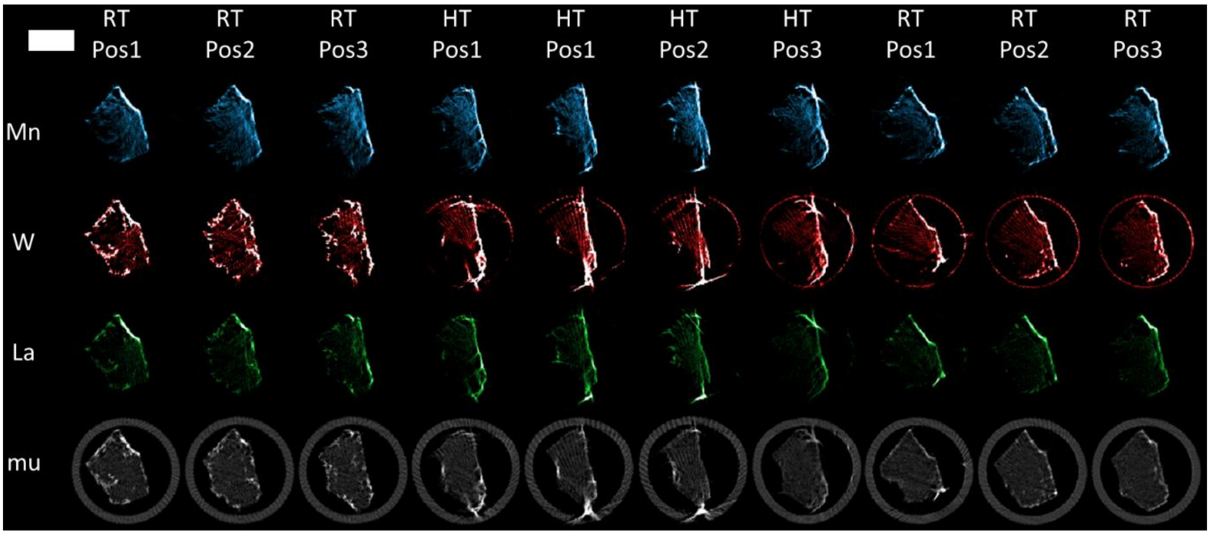

Figure 7: μ-XRF-CT scans of the 2 % La-2 % Mn-1.6 % Na-3.1 % W/SiO_2 catalyst – RT for room temperature scans, HT for high temperature scans (i.e. above 700 °C). μ-XRF-CT scans were performed at three different vertical positions (Position 1 to 3). Scale bar corresponds to 0.25 mm.

μ-XRD-CT

The results from the phase identification of the fresh 2 % La-2 % Mn-1.6 % Na-3.1 % W/SiO_2 catalyst are presented in Figure S31. The same crystalline phases were identified as in the XRD-CT experiments described in the previous section (i.e. cristobalite-low, tridymite-low, Na_2WO_4, Mn_2O_3 / Mn_7SiO_{12} and $La_4Mn_5Si_4O_{22}$). The data analysis strategy was identical to the one used for the μ-XRD-CT data of the 2 % Mn-1.6 % Na-3.1 % W/SiO_2 catalyst; a diffraction peak of interest was chosen for each crystalline phase present and then batch peak fitting of the μ-XRD-CT data was performed. These peaks of interest are summarised in Table S7.

The results from the peak fitting of the μ-XRD-CT data are presented in Figure 8 where the phase distribution maps of each component are shown. As expected, the crystalline SiO_2 phases (support of the catalyst) are homogeneously distributed and describe very accurately the catalyst particles in terms of both size and shape. This homogeneous distribution of the crystalline SiO_2 phases is consistent for all the μ-XRD-CT datasets (i.e. regardless of *z* position and temperature). More importantly, the Mn_2O_3/Mn_7SiO_{12} phases are also seen to be homogeneously distributed over the catalyst particles which is in full agreement with the XRD-CT data presented in the previous section (Figure 4).

On the other hand, the $La_4Mn_5Si_4O_{22}$ phase (i.e. the other crystalline Mn containing phase) is seen to be preferentially located near the surface of the catalyst particles which is also in agreement with the XRD-CT results presented previously in Figure 4. It is therefore consistent that the regions of high intensity in the La μ-XRF-CT maps presented in Figure 7 are co-located with the $La_4Mn_5Si_4O_{22}$ phase distribution map. The $NaLa(WO_4)_2$ phase is considered to be absent in the fresh catalyst when the summed diffraction pattern is used for the phase identification (Figure S31). However, the μ-XRD-CT data revealed that at certain regions at the surface of the catalyst particle, there is weak diffraction signal corresponding to the $NaLa(WO_4)_2$ phase. As it is clearly shown in Figures 7 and 8, the combination of the phase distribution maps of Na_2WO_4 and $NaLa(WO_4)_2$ correspond to the W XRF-CT map implying that the W containing species are mainly present in crystalline forms. These observations regarding the distribution of the Mn and Na_2WO_4 species obtained from these high-resolution images (Figures 7 and 8) are consistent with previous observations (Figure 4) that La promotion leads to a greater dispersion of the Mn species while Na_2WO_4 is located predominantly near the surface of the catalyst particles (i.e. following an egg shell distribution).

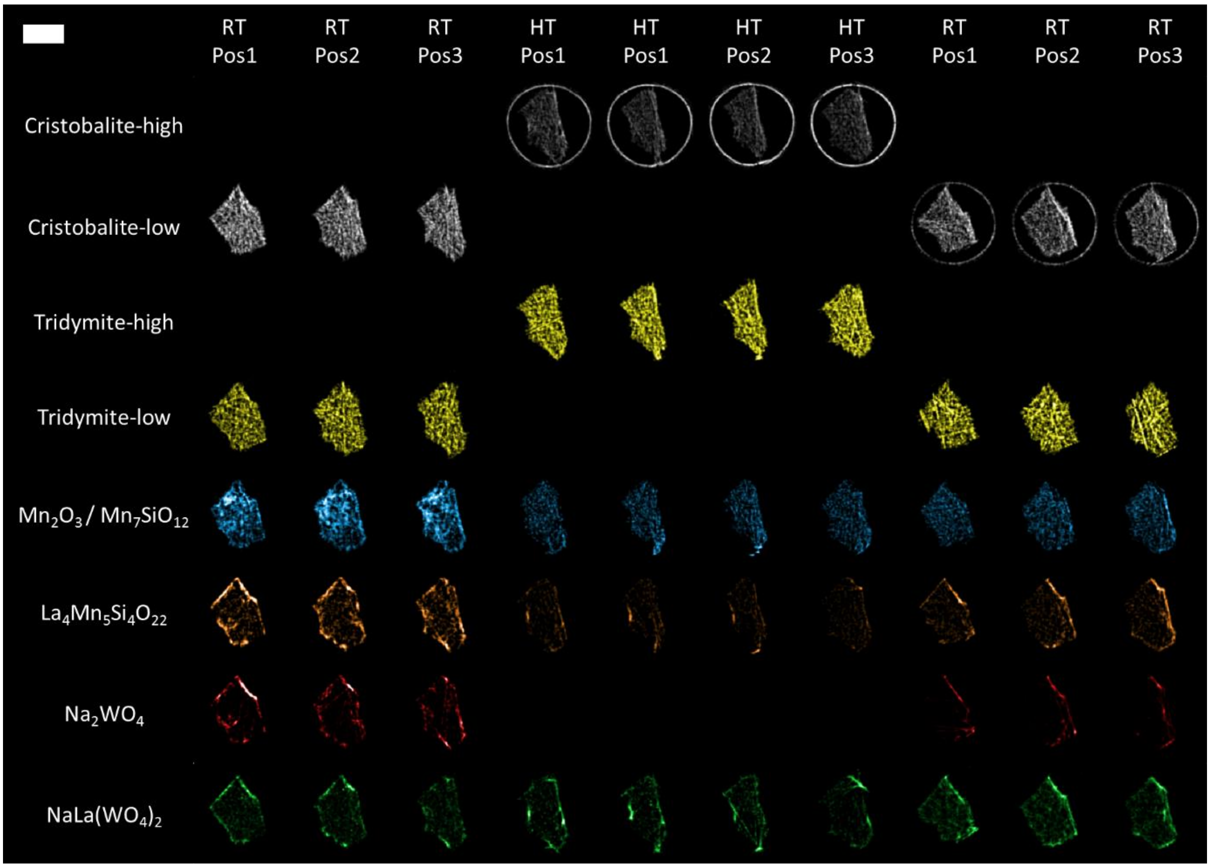

Figure 8: Phase distribution maps of the various crystalline phases present in the 2 % La-2 % Mn-1.6 % Na-3.1 % W/SiO_2 catalyst during the OCM experiment. Scale bar corresponds to 0.25 mm.

At high temperatures, a SiO_2 cristobalite ring is seen to form and grow with time at the inner side of the capillary. As thoroughly discussed in the previous section, this phenomenon is attributed to the loss of Na^+ species from the catalyst to the reactor vessel. It should be noted though that the La-promoted catalyst is seen to be more chemically stable compared to the unpromoted catalyst (more stable Na and W containing species). This is clearly indicated when the W XRF-CT maps of the two catalysts are directly compared. This claim is also supported from the fact that at the end of the OCM experiment with the La-promoted catalyst, there is no Na_2WO_4 present at the capillary but only at the catalyst particles (Figures 6 and 8).

As expected, the mass spectrometry data collected during the OCM experiment with the La-promoted catalyst show that the catalyst was captured in its active state. As it is shown in Figure S32, there is signal from masses corresponding to higher than CH_4 hydrocarbon molecules (i.e. m/z of 27 and 30) under reaction conditions (i.e. once the required temperature was reached) and that this signal remains present for the duration of the OCM experiment (i.e. no apparent deactivation of the La-promoted catalyst).

However, the loss of Na and W containing species from the 2 % La-2 % Mn-1.6 % Na-3.1 % W/SiO_2 catalyst (upon reaching the OCM required high temperatures) had an impact on the evolution of the crystalline phases containing these elements. More specifically, in contrast to the XRD-CT experiment presented in the previous section, the growth of the $NaLa(WO_4)_2$ phase was not that significant (Figure S33). In Figure S33, the summed diffraction patterns of all μ-XRD-CT datasets are presented. The Na_2WO_4 phase is seen to reform upon cooling to room temperature at the end of the OCM experiment but the diffraction signal generated by this phase has been significantly weakened. This also implied from the phase distribution maps of Na_2WO_4 presented in Figure 8. On the other hand, the Mn containing crystalline phases are behaving in accordance to the XRD-CT experiment of the same catalyst presented in the previous section. More specifically, the diffraction signal of both Mn_2O_3/Mn_7SiO_{12} and $La_4Mn_5Si_4O_{22}$ phases decreased under OCM reaction conditions but did not vanish. This should be expected as the Mn_2O_3/Mn_7SiO_{12} phases remained present even in the XRD-CT experiment presented in the previous section (Figure 4), where the OCM reaction mixtures tested were richer in CH_4 (i.e. very reducing chemical environment).

High temperature PXRD and *ex situ* PXRD and XRD-CT measurements

The behaviour of both the 2 % Mn-1.6 % Na-3.1 % W/SiO_2 and the 2 % La-2 % Mn-1.6 % Na-3.1 % W/SiO_2 catalysts was also investigated with high temperature powder diffraction measurements under inert environment (i.e. He flow of 30 ml min^{-1}) using a lab diffractometer. The purpose of these experiments was to identify which of the solid-state changes that take place in the catalysts at high temperatures (as observed from the synchrotron X-ray tomographic experiments) are attributed to the chemical environment (i.e. OCM reaction mixtures) and which are attributed to temperature (i.e. thermal effects). The results from the powder diffraction measurements of the 2 % Mn-1.6 % Na-3.1 % W/SiO_2 catalyst are presented in Figure 9.

At 600 °C, the lower symmetry orthorhombic Na_2WO_4 is present (apart from the cubic one) but upon reaching 700 °C there are no diffraction that can be attributed to any Na-W-O phases. This is expected and is in agreement with the results obtained from the lXRD-CT data presented previously (Figure S8). Furthermore, the diffraction signal corresponding to the Mn_2O_3/Mn_7SiO_{12} phases is seen to decrease with time at high temperatures. At this point it should be noted that the acquisition of each powder diffraction pattern lasted for approximately 2 h. This means that the solid-state changes taking place at high temperatures should not be simply tracked/treated as a function of temperature but as a function of both time and temperature (i.e. results of prolonged exposure of the catalyst to high temperatures).

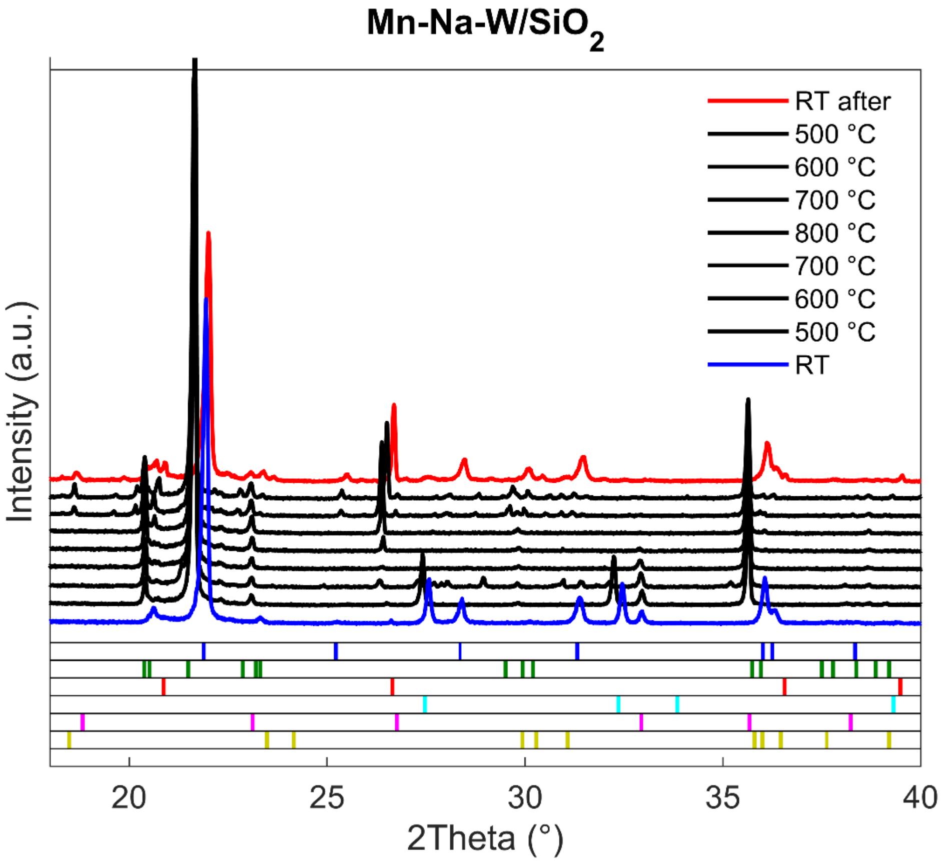

Figure 9: High temperature powder diffraction measurements of the 2 % Mn-1.6 % Na-3.1 % W/SiO_2 catalyst collected under He flow.

It is impressive that no Na_2WO_4 or Mn_2O_3/Mn_7SiO_{12} phases are observed in the catalyst at the end of the experiment. There are no crystalline Na containing phases and the only Mn/W crystalline phase present is $MnWO_4$. This result is crucial as it shows that the Mn species present in the Mn_2O_3/Mn_7SiO_{12} can be reduced from Mn^{3+} to Mn^{2+} at high temperatures even under He flow (thermal effect). This result also implies that the gases used in the calcination step during the preparation of the catalyst can have a strong impact on the state of the catalyst before the actual OCM experiment. To our knowledge this phenomenon has not been reported/investigated in literature in the past. Furthermore, it is seen that that there are significant solid-state changes taking place in the SiO_2 support of the catalyst. Tridymite, as expected, grows during this high temperature treatment of the 2 % Mn-1.6 % Na-3.1 %

W/SiO_2 catalyst but it is the increase in the diffraction signal corresponding to quartz that is most significant ($2\theta = 26.4$-$26.7°$).

A high temperature powder diffraction experiment under He flow was also performed with the 2 % La-2 % Mn-1.6 % Na-3.1 % W/SiO_2 catalyst. The results from these powder diffraction measurements are presented in Figure 10. As in the previous experiment with the unpromoted catalyst, at 600 °C, the lower symmetry orthorhombic Na_2WO_4 is present (apart from the cubic one) but upon reaching 700 °C there are no diffraction that can be attributed to any Na-W-O phases. This result was expected and is in agreement with the results obtained from the IXRD-CT data of the same catalyst (Figure S18). $NaLa(WO_4)_2$ is seen to be present at 700 °C and continues to grow in successively higher temperatures. By the end of the experiment, the diffraction signal generated by the Na_2WO_4, Mn_2O_3/Mn_7SiO_{12} and $La_4Mn_5Si_4O_{22}$ phases has diminished. The only crystalline phase present containing the active components of the catalyst is the $NaLa(WO_4)_2$ phase. Additionally, in contrast to the 2 % Mn-1.6 % Na-3.1 % W/SiO_2 catalyst, the diffraction signal generated by the SiO_2 quartz phase does not significantly change during this experiment. This result further supports the claim made in the previous section that one of the roles of La in this catalyst is to stabilise and supress the solid-state evolution the SiO_2 support.

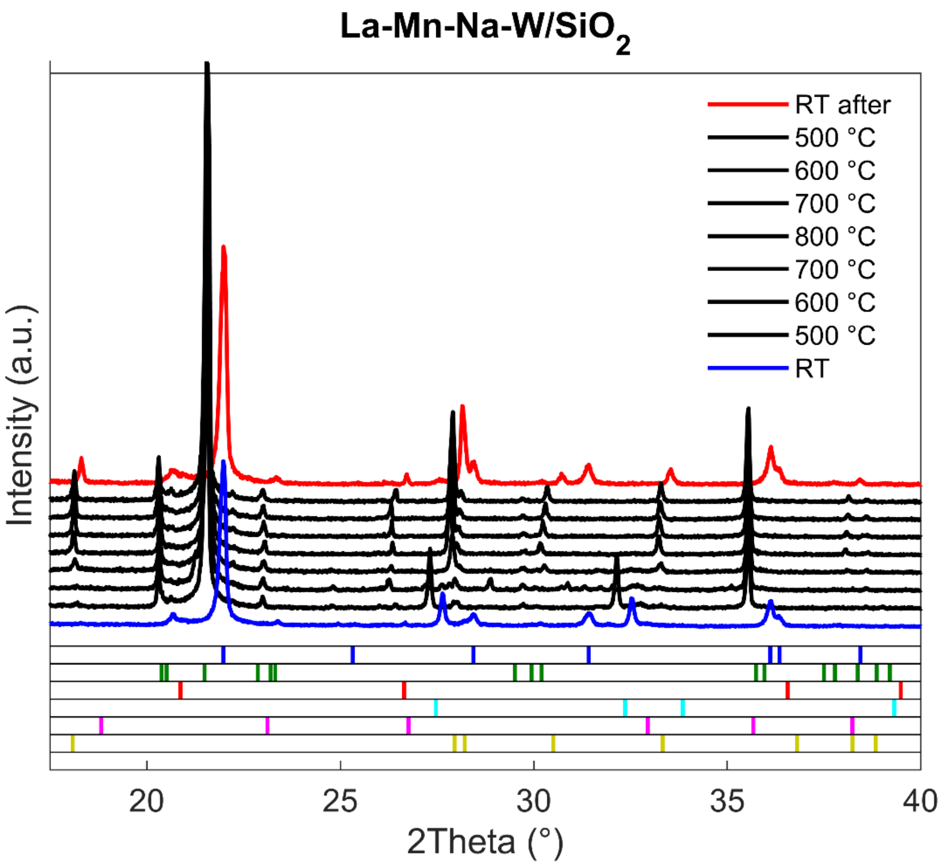

Figure 10: High temperature powder diffraction measurements of the 2 % La-2 % Mn-1.6 % Na-3.1 % W/SiO$_2$ catalyst collected under He flow.

Summary and Conclusions

In this study we presented the results from the first multi-length-scale chemical imaging study of unpromoted and La-promoted Mn-Na-W/SiO$_2$ catalysts under OCM reaction conditions. The catalysts were investigated from the reactor level (mm scale) down to the single catalyst particle level (µm scale) with different synchrotron X-ray based tomographic techniques (multi-modal CT experiments). The XRD-CT experiments revealed that both catalysts evolve under OCM operating conditions. More specifically, the unpromoted Mn-Na-W/SiO$_2$ catalyst is chemically unstable at high temperatures. The XRD-CT data suggested that there is loss of Na$^+$ from the catalyst particles as formation of cristobalite was observed at the SiO$_2$ capillary (reactor vessel). This claim was further supported by *ex situ* micro-CT and SEM/WDS measurements; the SEM/WDS measurements also suggested that W-containing species are leaving the catalyst during the OCM experiment. The loss of active components is attributed to the Na$_2$WO$_4$ phase which melts before reaching the required high temperatures for the OCM reaction and the various Na and W-containing species become both mobile and volatile.

It was also shown that crystalline Mn_2O_3 / Mn_7SiO_{12} is not an essential component to yield an active OCM catalyst; under very reducing environments the main crystalline phase was $MnWO_4$ and no changes in catalyst activity were observed though with the mass spectrometry data. The La-promoted catalyst was shown to be chemically stable; the Na and W species remained in the catalyst through the formation of new stable phase, identified as $NaLa(WO_4)_2$.

The multi-modal CT experiments proved that the solid-state chemistry results obtained from the XRD-CT experiments presented in the previous section are directly reproducible and also revealed new information regarding the parameters that affect the chemical evolution of both catalysts. It was shown that the behaviour of both catalysts strongly depends on the catalyst pre-treatment (i.e. thermal) and the OCM reaction mixture used. For example, the Mn_2O_3 / Mn_7SiO_{12} crystalline phases can remain stable/present under OCM reaction conditions for a longer period of time if the reaction mixture is not very rich in CH_4 (in very reducing environments the Mn species will be reduced from Mn^{3+} to Mn^{2+} and form the $MnWO_4$ phase). Additionally, the Na and W containing species can become unstable in the La-promoted catalyst if the temperature of the system is increased rapidly as there is a certain time period needed to for the $NaLa(WO_4)_2$ to form and grow.

Supplementary high temperature PXRD experiments in an inert chemical environment (i.e. He) and *ex situ* PXRD and XRD-CT experiments showed that the formation/growth of the $NaLa(WO_4)_2$ phase is a temperature driven phenomenon. It is a result of thermal treatment of the catalyst and its formation does not depend on the chemical environment present (i.e. purely thermal phenomenon). It can be concluded that in order to have a chemically stable catalyst, it is essential to stabilize the Na^+ and WO_4^{2-} ions at the high temperatures required for the OCM reaction. The multi-length-scale chemical CT experiments presented in this study showed that the La can play this role by trapping the mobile/volatile Na^+ and WO_4^{2-} species by forming this new crystalline phase ($NaLa(WO_4)_2$). More importantly, these new results is a major breakthrough in the OCM catalyst design; not only the integrity of catalyst is maintained during the operating conditions but also the catalyst activity is not impaired by the addition of the La components [32,33]. The latter could be attributed to the fact that the OCM reaction process is generally accepted to be based on methane activation at the catalyst surface and gas-phase recombination of methyl radicals. It is therefore implied that in the La-promoted catalyst, since the methane activation rate is not affected in a negative manner, the La-containing species do not directly alter the active catalyst surface species (i.e. absent from surface / buried away from surface) or the methane delivery rate to the catalyst is not overwhelming under the applied operating conditions.

The spatially-resolved signals obtained from the synchrotron chemical CT experiments revealed how the La promoter enhances the catalyst performance. Specifically, it was shown that the La promoter plays a quadruple role:

1) It acts as a structural promoter by enabling the formation of the stable $NaLa(WO_4)_2$ phase

2) It acts a chemical promoter by enhancing the metal-support interaction. This could be observed indirectly through the formation of a $La_4Mn_5Si_4O_{22}$ phase, clearly indicating the direct interaction of the Mn species with the SiO_2 support. Mn species in the formed $La_4Mn_5Si_4O_{22}$ phase were shown to be more stable when compared to pure Mn_2O_3.

3) It improves the dispersion of the Mn species over the support (homogeneous distribution of the Mn_2O_3 / Mn_7SiO_{12} phases in the catalyst particles).

4) It stabilises the SiO_2 support by suppressing its evolution at high temperatures. This is probably achieved indirectly by trapping the mobile Na^+ species which are responsible for the transformation of amorphous SiO_2 to various crystalline phases at these relatively low temperatures (ca. 800 °C).

It should be emphasized that it was the real-time characterisation coupled with the spatially-resolved signals obtained from the chemical tomographic techniques that allowed us to unravel the multiple roles of the La promoter. Furthermore, after more than three decades of experiments, this is the first time direct evidence is provided showing the neither crystalline Mn_2O_3 / Mn_7SiO_{12} or $MnWO_4$ species are required components to yield an active catalyst. This implies that nano or non-crystalline Mn species are the ones directly participating in the active catalyst sites. This has direct implications on how future experiments with this type of catalyst should be designed. As an example, one may consider the application of Pair Distribution Function Computed Tomography (PDF-CT) or Energy Dispersive X-ray Absorption Spectroscopy Computed Tomography (ED-XAS-CT) as complimentary techniques to study the amorphous/nano-crystalline species in these multi-component catalyst systems [49,88].

Supporting Information

1. Experimental details
2. Strategy for the Rietveld analysis of XRD-CT data
3. Glass signal removal strategy from the temporal XRD data
4. Experimental conditions – OCM experiment with unpromoted Mn-Na-W/SiO_2 catalyst (XRD-CT at ID15)
5. Initial composition of unpromoted Mn-Na-W/SiO_2 catalyst (XRD-CT at ID15)
6. Temperature ramp and OCM operating conditions with unpromoted Mn-Na-W/SiO_2 catalyst (XRD-CT at ID15)
7. Composition of spent unpromoted Mn-Na-W/SiO_2 catalyst (XRD-CT at ID15)
8. Weight fraction maps of fresh and spent unpromoted Mn-Na-W/SiO_2 catalyst (XRD-CT at ID15A)
9. Experimental conditions – OCM experiment with La promoted Mn-Na-W/SiO_2 catalyst (XRD-CT at ID15)
10. Initial composition of La promoted Mn-Na-W/SiO_2 catalyst (XRD-CT at ID15)
11. Temperature ramp and OCM operating conditions with La promoted Mn-Na-W/SiO_2 catalyst (XRD-CT at ID15)
12. Composition of spent La promoted Mn-Na-W/SiO_2 catalyst (XRD-CT at ID15)
13. Weight fraction maps of fresh and La-promoted Mn-Na-W/SiO2 catalyst (XRD-CT at ID15A)
14. Ex situ X-ray micro-CT and SEM/WDS measurements
15. Strategy for XRF-CT data reconstruction (µXRF/XRD-CT at I18)
16. Initial composition of unpromoted Mn-Na-W/SiO_2 catalyst (µXRF/XRD-CT at I18)
17. OCM operating conditions with unpromoted Mn-Na-W/SiO_2 catalyst (µXRF/XRD-CT at I18)
18. Initial composition of La promoted Mn-Na-W/SiO_2 catalyst (µXRF/XRD-CT at I18)
19. OCM operating conditions with La promoted Mn-Na-W/SiO_2 catalyst (µXRF/XRD-CT at I18)
20. Ex situ XRD-CT measurements at ID11 and ID31, ESRF
21. High temperature treatment of unpromoted Mn-Na-W/SiO_2 catalyst
22. High temperature treatment of La promoted Mn-Na-W/SiO_2 catalyst

23. Ex situ X-ray fluorescence measurements

24. Summary of physico-chemical catalyst evolution

Acknowledgments

The development of the catalyst used in this work was funded within the DEMCAMER project as part of the European Union Seventh Framework Programme (FP7/2007–2013) under grant agreement no. NMP3-LA-2011–262840. Note: 'The present publications reflect only the authors' views and the Union is not liable for any use that may be made of the information contained therein'. The authors would like to thank the ESRF (ch4149, ch4312 and ch4455 proposals) and Diamond for beamtime. The authors would also like to thank the John Wright from beamline ID11 and Jakub Drnec from beamline Id31 for their help during the beamtime experiments. Antonis Vamvakeros and Dorota Matras (respectfully in full and in part) are supported through funding received from the European Union Horizon 2020 research and innovation programme under grant agreement no. 679933 (MEMERE project). Andrew M. Beale acknowledges EPSRC (grant EP/K007467/1) for an Early Career Fellowship. The authors would like to thank Thomas Buslaps and Denis Duran for their help during the experimental setups at beamline ID15A.

References

1 O. C. D. Anejionu, J. D. Whyatt, G. A. Blackburn and C. S. Price, *Atmos. Environ.*, 2015, **118**, 184–193.

2 R. A. Kerr, *Science (80-.).*, 2010, **328**, 1624–1626.

3 J. Shan, M. Li, L. F. Allard, S. Lee and M. Flytzani-Stephanopoulos, *Nature*, 2017, **551**, 605.

4 J. H. Lunsford, *Catal. Today*, 2000, **63**, 165–174.

5 E. McFarland, *Science (80-.).*, 2012, **338**, 340–342.

6 A. Cruellas, J. J. Bakker, M. van Sint Annaland, J. A. Medrano and F. Gallucci, *Energy Convers. Manag.*, 2019, **198**, 111789.

7 A. Galadima and O. Muraza, *J. Ind. Eng. Chem.*, 2016, **37**, 1–13.

8 P. Tang, Q. Zhu, Z. Wu and D. Ma, *Energy Environ. Sci.*, 2014, **7**, 2580–2591.

9 Y. Gao, L. Neal, D. Ding, W. Wu, C. Baroi, A. M. Gaffney and F. Li, *ACS Catal.*, 2019, **9**, 8592–8621.

10 C. Karakaya and R. J. Kee, *Prog. Energy Combust. Sci.*, 2016, **55**, 60–97.

11 M. C. Alvarez-Galvan, N. Mota, M. Ojeda, S. Rojas, R. M. Navarro and J. L. G. Fierro, *Catal. Today*, 2011, **171**, 15–23.

12 K. Takanabe, *J. Japan Pet. Inst.*, 2012, **55**, 1–12.

13 S. Arndt, T. Otremba, U. Simon, M. Yildiz, H. Schubert and R. Schomäcker, *Appl. Catal. A Gen.*, 2012, **425**–**426**, 53–61.

14 D. Kiani, S. Sourav, J. Baltrusaitis and I. E. Wachs, *ACS Catal.*, 2019, **9**, 5912–5928.

15 D. X. Fang, X. P.; Li, S. B.; Lin, J. Z.; Gu, J. F.; Yang, *J. Mol. Catal.*

16 Y. . Fang, X.; Li, S.; Lin, J.; Chu, *J. Mol. Catal.*, 1992, **6**, 427–433.

17 J. A. Sofranko, J. J. Leonard and C. A. Jones, *J. Catal.*, 1987, **103**, 302–310.

18 S. Ji, T. Xiao, S. Li, C. Xu, R. Hou, K. S. Coleman and M. L. H. Green, *Appl. Catal. A Gen.*, 2002, **225**, 271–284.

19 D. J. Wang, M. P. Rosynek and J. H. Lunsford, *J. Catal.*, 1995, **155**, 390–402.

20 S. Pak and J. H. Lunsford, *Appl. Catal. A Gen.*, 1998, **168**, 131–137.

21 Z. C. Jiang, C. J. Yu, X. P. Fang, S. Ben Li and H. L. Wang, *J. Phys. Chem.*, 1993, **97**, 12870–12875.

22 J. Wu, S. Li, J. Niu and X. Fang, *Appl. Catal. A Gen.*, 1995, **124**, 9–18.

23 Z. Jiang, H. Gong and S. Li, in *Spillover and Migration of Surface Species on Catalysts*, eds. C. Li and Q. B. T.-S. in S. S. and C. Xin, Elsevier, 1997, vol. 112, pp. 481–490.

24 V. Fleischer, R. Steuer, S. Parishan and R. Schomäcker, *J. Catal.*, 2016, **341**, 91–103.

25 V. Fleischer, U. Simon, S. Parishan, M. G. Colmenares, O. Görke, A. Gurlo, W. Riedel, L. Thum, J. Schmidt, T. Risse, K.-P. Dinse and R. Schomäcker, *J. Catal.*, 2018, **360**, 102–

117.

26 A. Palermo, J. P. Holgado Vazquez, A. F. Lee, M. S. Tikhov and R. M. Lambert, *J. Catal.*, 1998, **177**, 259–266.

27 S. Li, *J. Nat. Gas Chem.*, 2003, **12**, 1–9.

28 J. Lin, J. Gu, D. Yang, C. Zhang, Y. Yang, Y. Chu and S. Li, *Shiyou Huagong/Petrochemical Technol.*, 1995, **24**, 293–298.

29 J. Wang, L. Chou, B. Zhang, H. Song, J. Zhao, J. Yang and S. Li, *J. Mol. Catal. A Chem.*, 2006, **245**, 272–277.

30 J. S. Ahari, M. T. Sadeghi and S. Zarrinpashne, *J. Nat. Gas Chem.*, 2011, **20**, 204–213.

31 J. Wu, H. Zhang, S. Qin and C. Hu, *Appl. Catal. A Gen.*, 2007, **323**, 126–134.

32 I. Ismagilov, E. Matus, M. Kerzhentsev, I. Prosvirin, R. Navarro, J. Fierro, G. Gerritsen, E. Abbenhuis and Z. Ismagilov, *Eurasian Chem. J.*, , DOI:10.18321/ectj201.

33 I. Z. Ismagilov, E. V Matus, S. D. Vasil’ev, V. V Kuznetsov, M. A. Kerzhentsev and Z. R. Ismagilov, *Kinet. Catal.*, 2015, **56**, 456–465.

34 R. Ghose, H. T. Hwang and A. Varma, *Appl. Catal. A Gen.*, 2014, **472**, 39–46.

35 A. M. Beale, S. D. M. Jacques and B. M. Weckhuysen, *Chem. Soc. Rev.*, 2010, **39**, 4656–4672.

36 J.-D. Grunwaldt and C. G. Schroer, *Chem. Soc. Rev.*, 2010, **39**, 4741–4753.

37 J.-D. Grunwaldt, J. B. Wagner and R. E. Dunin-Borkowski, *ChemCatChem*, 2013, **5**, 62–80.

38 A. M. Beale, S. D. M. Jacques, E. K. Gibson and M. Di Michiel, *Coord. Chem. Rev.*, 2014, **277**–**278**, 208–223.

39 Z. Ristanović and B. M. Weckhuysen, *Angew. Chemie Int. Ed.*, 2014, **53**, 8556–8558.

40 N. E. Tsakoumis, A. P. E. York, D. Chen and M. Rønning, *Catal. Sci. Technol.*, 2015, **5**, 4859–4883.

41 A. Urakawa, *Curr. Opin. Chem. Eng.*, 2016, **12**, 31–36.

42 F. Meirer and B. M. Weckhuysen, *Nat. Rev. Mater.*, 2018, **3**, 324–340.

43 A. Vamvakeros, S. D. M. Jacques, M. Di Michiel, D. Matras, V. Middelkoop, I. Z. Ismagilov, E. V. Matus, V. V. Kuznetsov, J. Drnec, P. Senecal and A. M. Beale, *Nat. Commun.*, 2018, **9**, 4751.

44 R. Portela, S. Perez-Ferreras, A. Serrano-Lotina and M. A. Bañares, *Front. Chem. Sci. Eng.*, 2018, **12**, 509–536.

45 T. M. M. Heenan, C. Tan, J. Hack, D. J. L. Brett and P. R. Shearing, *Mater. Today*, , DOI:https://doi.org/10.1016/j.mattod.2019.05.019.

46 S. D. M. Jacques, M. Di Michiel, A. M. Beale, T. Sochi, M. G. O'Brien, L. Espinosa-Alonso, B. M. Weckhuysen and P. Barnes, *Angew. Chemie Int. Ed.*, 2011, **50**, 10148–10152.

47 M. G. O'Brien, S. D. M. Jacques, M. Di Michiel, P. Barnes, B. M. Weckhuysen and A. M. Beale, *Chem. Sci.*, 2012, **3**, 509–523.

48 T. Saida, O. Sekizawa, N. Ishiguro, M. Hoshino, K. Uesugi, T. Uruga, S. Ohkoshi, T. Yokoyama and M. Tada, *Angew. Chemie Int. Ed.*, 2012, **51**, 10311–10314.

49 S. D. M. Jacques, M. Di Michiel, S. A. J. Kimber, X. Yang, R. J. Cernik, A. M. Beale and S. J. L. Billinge, *Nat. Commun.*, 2013, **4**, 2536.

50 A. M. Beale, E. K. Gibson, M. G. O'Brien, S. D. M. Jacques, R. J. Cernik, M. Di Michiel, P. D. Cobden, Ö. Pirgon-Galin, L. van de Water, M. J. Watson and B. M. Weckhuysen, *J. Catal.*, 2014, **314**, 94–100.

51 S. W. T. Price, K. Ignatyev, K. Geraki, M. Basham, J. Filik, N. T. Vo, P. T. Witte, A. M. Beale and J. F. W. Mosselmans, *Phys. Chem. Chem. Phys.*, 2015, **17**, 521–529.

52 D. S. Wragg, M. G. O'Brien, M. Di Michiel and F. Lonstad-Bleken, *J. Appl. Crystallogr.*, 2015, **48**, 1719–1728.

53 S. W. T. Price, K. Geraki, K. Ignatyev, P. T. Witte, A. M. Beale and J. F. W. Mosselmans, *Angew. Chemie*, 2015, **127**, 10024–10027.

54 T. L. Sheppard, S. W. T. Price, F. Benzi, S. Baier, M. Klumpp, R. Dittmeyer, W.

Schwieger and J.-D. Grunwaldt, *J. Am. Chem. Soc.*, 2017, **139**, 7855–7863.

55 P. Senecal, S. D. M. Jacques, M. Di Michiel, S. A. J. Kimber, A. Vamvakeros, Y. Odarchenko, I. Lezcano-Gonzalez, J. Paterson, E. Ferguson and A. M. Beale, *ACS Catal.*, , DOI:10.1021/acscatal.6b03145.

56 S. W. T. Price, D. J. Martin, A. D. Parsons, W. A. Sławiński, A. Vamvakeros, S. J. Keylock, A. M. Beale and J. F. W. Mosselmans, *Sci. Adv.*, , DOI:10.1126/sciadv.1602838.

57 H. Matsui, N. Ishiguro, T. Uruga, O. Sekizawa, K. Higashi, N. Maejima and M. Tada, *Angew. Chemie Int. Ed.*, 2017, **56**, 9371–9375.

58 A. M. Beale, S. D. M. Jacques, M. Di Michiel, F. W. Mosselmans, S. W. T. Price, P. Senecal, A. Vamvakeros and J. Paterson, *Philos. Trans. R. Soc. A Math. Phys. Eng. Sci.*, , DOI:10.1098/rsta.2017.0057.

59 M. Hirose, N. Ishiguro, K. Shimomura, N. Burdet, H. Matsui, M. Tada and Y. Takahashi, *Angew. Chemie*, 2018, **130**, 1490–1495.

60 T. Li, T. M. M. Heenan, M. F. Rabuni, B. Wang, N. M. Farandos, G. H. Kelsall, D. Matras, C. Tan, X. Lu, S. D. M. Jacques, D. J. L. Brett, P. R. Shearing, M. Di Michiel, A. M. Beale, A. Vamvakeros and K. Li, *Nat. Commun.*, , DOI:10.1038/s41467-019-09427-z.

61 Y. De Vos, A. Vamvakeros, D. Matras, M. Jacobs, P. Van Der Voort, I. Van Driessche, S. Jacques, V. Middelkoop and A. Verberckmoes, *Int. J. Greenh. Gas Control*, , DOI:10.1016/j.ijggc.2019.06.016.

62 V. Middelkoop, A. Vamvakeros, D. de Wit, S. D. M. Jacques, S. Danaci, C. Jacquot, Y. de Vos, D. Matras, S. W. T. Price and A. M. Beale, *J. CO2 Util.*, 2019, **33**, 478–487.

63 I. Martens, A. Vamvakeros, R. Chattot, M. V. Blanco, M. Rasola, J. Pusa, S. D. M. Jacques, D. Bizzotto, D. P. Wilkinson, B. Ruffmann, S. Heidemann, V. Honkimäki and J. Drnec, *J. Power Sources*, , DOI:10.1016/j.jpowsour.2019.226906.

64 D. P. Finegan, A. Vamvakeros, L. Cao, C. Tan, T. M. M. Heenan, S. R. Daemi, S. D. M. Jacques, A. M. Beale, M. Di Michiel, K. Smith, D. J. L. Brett, P. R. Shearing and C. Ban,

Nano Lett., , DOI:10.1021/acs.nanolett.9b00955.

65 J. Hester, *J. Appl. Crystallogr.*, 2006, **39**, 621–625.

66 D. Matras, A. Vamvakeros, S. Jacques, N. Grosjean, B. Rollins, S. Poulston, G. B. G. Stenning, H. Godini, J. Drnec, R. J. Cernik and A. M. Beale, *Faraday Discuss.*, , DOI:10.1039/C9FD00142E.

67 D. Matras, S. D. M. Jacques, H. R. Godini, M. Khadivi, J. Drnec, A. Poulain, R. J. Cernik and A. M. Beale, *J. Phys. Chem. C*, 2018, **122**, 2221–2230.

68 D. Matras, S. D. M. Jacques, S. Poulston, N. Grosjean, C. Estruch Bosch, B. Rollins, J. Wright, M. Di Michiel, A. Vamvakeros, R. J. Cernik and A. M. Beale, *J. Phys. Chem. C*, 2019, **123**, 1751–1760.

69 A. Vamvakeros, S. D. M. Jacques, V. Middelkoop, M. Di Michiel, C. K. Egan, I. Z. Ismagilov, G. B. M. Vaughan, F. Gallucci, M. Van Sint Annaland, P. R. Shearing, R. J. Cernik and A. M. Beale, *Chem. Commun.*, 2015, **51**, 12752–12755.

70 G. B. M. Vaughan, R. Baker, R. Barret, J. Bonnefoy, T. Buslaps, S. Checchia, D. Duran, F. Fihman, P. Got, J. Kieffer, S. A. J. Kimber, K. Martel, C. Morawe, D. Mottin, E. Papillon, S. Petitdemange, A. Vamvakeros, J.-P. Vieux and M. Di Michiel, *J. Synchrotron Radiat.*

71 A. Vamvakeros, S. D. M. Jacques, M. Di Michiel, P. Senecal, V. Middelkoop, R. J. Cernik and A. M. Beale, *J. Appl. Crystallogr.*, , DOI:10.1107/S160057671600131X.

72 A. Vamvakeros, S. D. M. Jacques, M. Di Michiel, V. Middelkoop, C. K. Egan, R. J. Cernik and A. M. Beale, *J. Appl. Crystallogr.*, , DOI:10.1107/S1600576715020701.

73 W. van Aarle, W. J. Palenstijn, J. De Beenhouwer, T. Altantzis, S. Bals, K. J. Batenburg and J. Sijbers, *Ultramicroscopy*, 2015, **157**, 35–47.

74 M. A. Newton, S. Checchia, A. J. Knorpp, D. Stoian, W. van Beek, H. Emerich, A. Longo and J. A. van Bokhoven, *Catal. Sci. Technol.*, 2019, **9**, 3081–3089.

75 S. Frolich and H. Birkedal, *J. Appl. Crystallogr.*, 2015, **48**, 2019–2025.

76 T. P. Tiemersma, M. J. Tuinier, F. Gallucci, J. A. M. Kuipers and M. van S. Annaland, *Appl. Catal. A Gen.*, 2012, **433**–**434**, 96–108.

77 M. Yildiz, Y. Aksu, U. Simon, T. Otremba, K. Kailasam, C. Göbel, F. Girgsdies, O. Görke, F. Rosowski, A. Thomas, R. Schomäcker and S. Arndt, *Appl. Catal. A Gen.*, 2016, **525**, 168–179.

78 S. Sadjadi, S. Jašo, H. R. Godini, S. Arndt, M. Wollgarten, R. Blume, O. Görke, R. Schomäcker, G. Wozny and U. Simon, *Catal. Sci. Technol.*, 2015, **5**, 942–952.

79 V. Salehoun, A. Khodadadi, Y. Mortazavi and A. Talebizadeh, *Chem. Eng. Sci.*, 2008, **63**, 4910–4916.

80 U. Simon, O. Görke, A. Berthold, S. Arndt, R. Schomäcker and H. Schubert, *Chem. Eng. J.*, 2011, **168**, 1352–1359.

81 S. Hou, Y. Cao, W. Xiong, H. Liu and Y. Kou, *Ind. Eng. Chem. Res.*, 2006, **45**, 7077–7083.

82 M. Sinev, E. Ponomareva, I. Sinev, V. Lomonosov, Y. Gordienko, Z. Fattakhova and D. Shashkin, *Catal. Today*, 2019, **333**, 36–46.

83 S. B. HOLMQUIST, *J. Am. Ceram. Soc.*, 1961, **44**, 82–86.

84 A. M. Venezia, V. La Parola, A. Longo and A. Martorana, *J. Solid State Chem.*, 2001, **161**, 373–378.

85 Y. SHINOHARA and N. KOHYAMA, *Ind. Health*, 2004, **42**, 277–285.

86 L. Zhao, N. Li, A. Langner, M. Steinhart, T. Y. Tan, E. Pippel, H. Hofmeister, K.-N. Tu and U. Gösele, *Adv. Funct. Mater.*, 2007, **17**, 1952–1957.

87 S. s. Cole, *J. Am. Ceram. Soc.*, 1935, **18**, 149–154.

88 D. F. Sanchez, A. S. Simionovici, L. Lemelle, V. Cuartero, O. Mathon, S. Pascarelli, A. Bonnin, R. Shapiro, K. Konhauser, D. Grolimund and P. Bleuet, *Sci. Rep.*, 2017, **7**, 16453.

Table of Contents/Abstract Graphics:

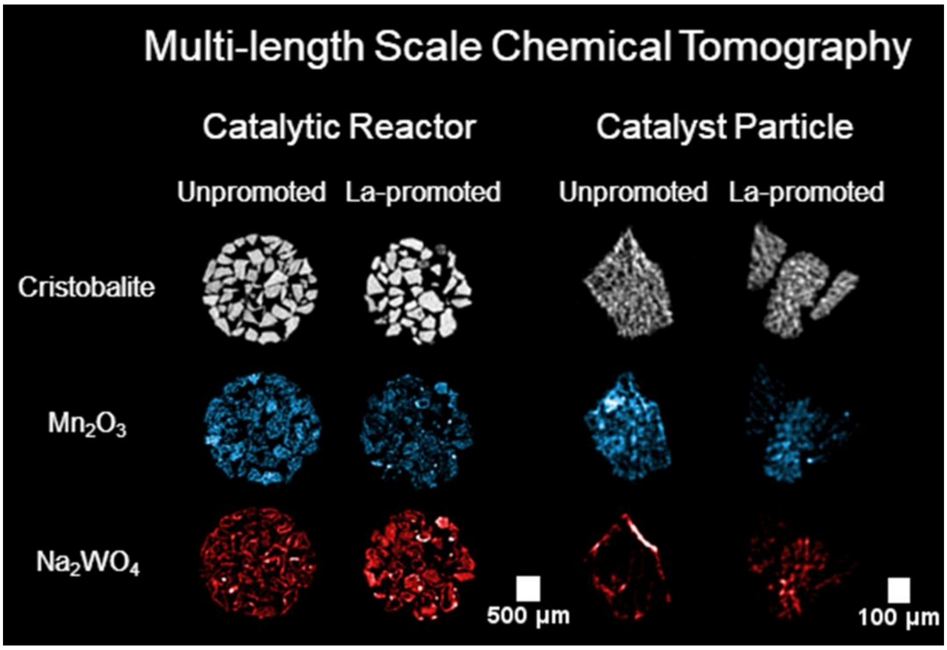
Multi-length Scale Chemical Tomography
Catalytic Reactor
Catalyst Particle
Unpromoted
La-promoted
Unpromoted
La-promoted
Cristobalite
Mn_2O_3
Na_2WO_4
500 µm
100 µm